# Numerical analysis of interseismic, coseismic and post-seismic phases for normal and reverse faulting earthquakes in Italy

Matteo Albano [1], Salvatore Barba,[1] Christian Bignami,[1] Eugenio Carminati,[2]
Carlo Doglioni,[1] Marco Moro,[1] Michele Saroli,[1,3] Sergey Samsonov[4] and
Salvatore Stramondo[1]

[1]*Istituto Nazionale di Geofisica e Vulcanologia, via di Vigna Murata* 605, 00143 *Roma, Italy. E-mail:* matteo.albano@ingv.it
[2]*Dipartimento di Scienze della Terra, 'Sapienza' Università di Roma, Piazzale Aldo Moro 5, 00185 Roma, Italy*
[3]*Dipartimento di Ingegneria Civile e Meccanica, Università degli Studi di Cassino e del Lazio meridionale, via G. di Biasio 43, 03043 Cassino (FR), Italy*
[4]*Canada Centre for Mapping and Earth Observation, Natural Resources Canada,* 560 *Rochester Street, Ottawa, ON K*1*A* 0*E*4*, Canada*

## SUMMARY

The preparation, initiation and occurrence dynamics of earthquakes in Italy are governed by several frequently unknown physical mechanisms and parameters. Understanding these mechanisms is crucial for developing new techniques and approaches for earthquake monitoring and hazard assessments. Here, we develop a first-order numerical model simulating quasi-static crustal interseismic loading, coseismic brittle episodic dislocation and post-seismic relaxation for extensional and compressional earthquakes in Italy based on a common framework of lithostatic and tectonic forces. Our model includes an upper crust, where the fault is locked, and a deep crust, where the fault experiences steady shear.

The results indicate that during the interseismic phase, the contrasting behaviour between the upper locked fault segment and lower creeping fault segment generates a stretched volume at depth in the hangingwall via extensional tectonics while a contracted volume forms via compressional tectonics. The interseismic stress and strain gradients invert at the coseismic stage, with the interseismic dilated volume contracting during the coseismic stage, and vice versa. Moreover, interseismic stress gradients promote coseismic gravitational subsidence of the hangingwall for normal fault earthquakes and elastic uplift for reverse fault earthquakes. Finally, the post-seismic relaxation is characterized by further ground subsidence and uplift for normal and reverse faulting earthquakes, respectively, which is consistent with the faulting style. The fault is the passive feature, with slipping generating the seismic waves, whereas the energy activating the movement is stored mostly in the hangingwall volume. The main source of energy for normal faulting and thrust is provided by the lithostatic load and elastic load, respectively.

**Key words:** Radar interferometry; Seismic cycle; Space geodetic surveys; Numerical modelling; Earthquake dynamics.

## 1 INTRODUCTION

The present-day geodynamic setting of the Apennines is related to the 'westward' subduction of the Adriatic plate beneath peninsular Italy (Carminati & Doglioni 2012; Carminati *et al.* 2012). The Central and Northern Apennines mountain belt evolved since Late Eocene–Oligocene times through the ENE to NNE migration of the thrust fronts, which was contemporaneous to the backarc opening of the Tyrrhenian sea due to the 'eastward' lithospheric slab retreat of the Adriatic plate (Doglioni *et al.* 1999; Meletti *et al.* 2000; Patacca & Scandone 2001). GPS data and seismicity distribution and geological and geophysical observations (Palano 2015; Devoti

*et al.* 2017) highlight the presence of at least two opposing tectonic regimes that coexist at short distances (Fig. 1a). Extensional tectonics characterizes the central and northern Apennines, whereas crustal shortening characterizes the Po plain and the Adriatic foreland (Chiarabba *et al.* 2015; Devoti *et al.* 2017). This tectonic setting is typical of subduction zones where the slab hinge moves away with respect to the upper plate (Doglioni *et al.* 2007), generating a low topography shallow accretionary prism above the slab hinge and a contemporaneous rifting in the hangingwall of the subduction characterized by higher topography (Doglioni *et al.* 1999). Moreover, high topography favours extensional seismicity whereas low topography favours contractional seismicity due to the opposite sign of
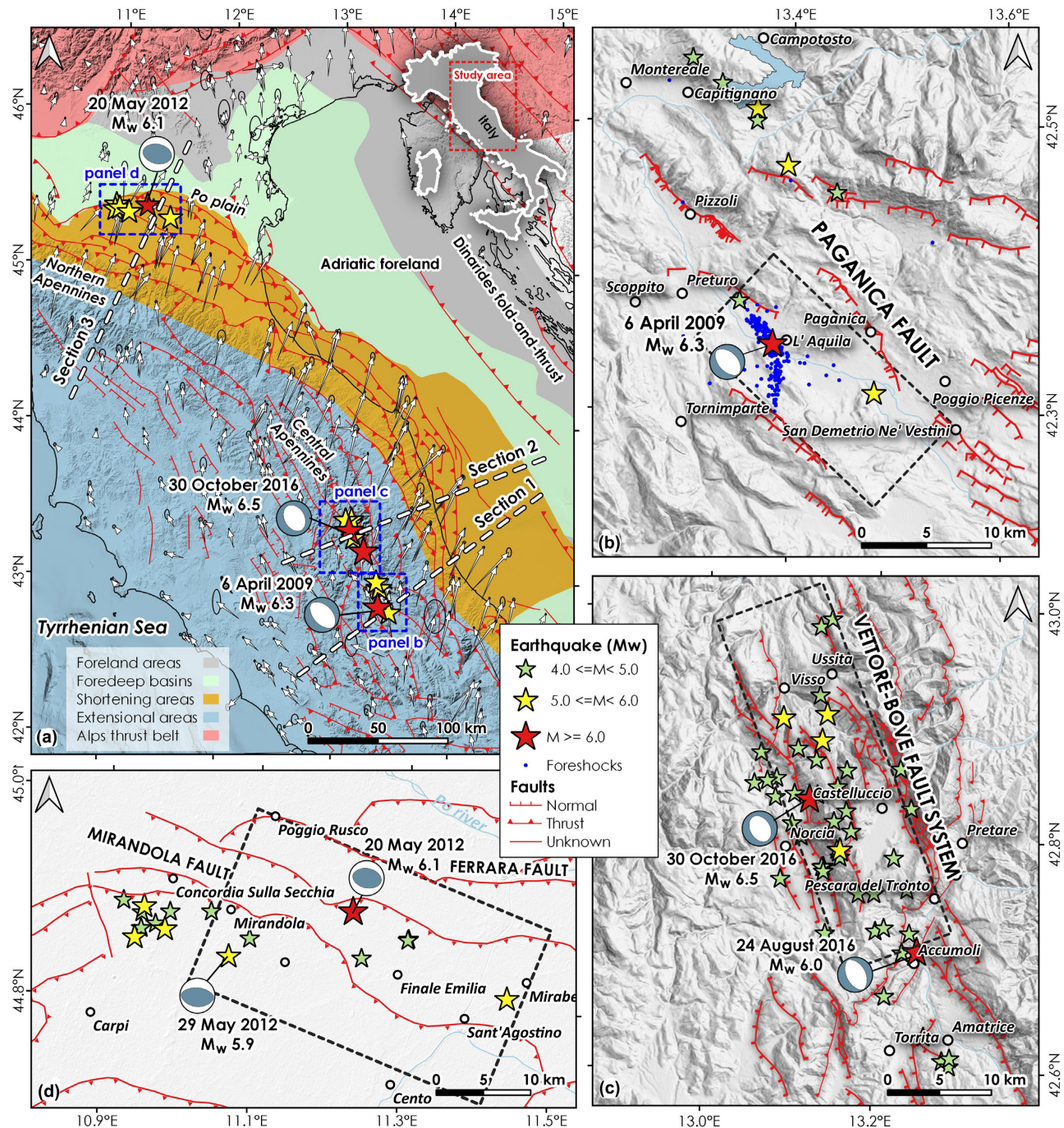
**Figure 1.** Tectonic sketch of the study area. (a) Simplified tectonic map showing the major tectonic and geodynamic setting of the region (modified from Carminati & Doglioni 2012; Petricca *et al.* 2015) with the locations of the studied earthquakes and the footprints of panels (b)–(d). The white arrows identify the interseismic horizontal velocities at GPS sites with respect to a fixed Eurasian frame (with 95 per cent error ellipses; for information about the GPS processing, refer to Devoti *et al.* 2017). (b) L'Aquila 2009 seismic sequence. (c) Norcia 2016 seismic sequence. (d) Emilia 2012 seismic sequence. The black rectangles in panels (b)–(d) indicate the projection at the surface of the fault planes responsible for the three events estimated from an analytical inversion of geodetic data (Atzori *et al.* 2009; Cheloni *et al.* 2016, 2019).

the lithostatic load in the two tectonic settings (Carminati *et al.* 2004).

Seismicity is dictated by the kinematics of the area, with dominant normal fault earthquakes along the elevated Central and Northern Apennines chain, whereas reverse fault earthquakes occur in the low land Po plain and the Adriatic foreland. Among the numerous

seismogenic normal and thrust faults, some of them generated damaging earthquakes in the last century, with magnitudes up to 7 (e.g. Avezzano 1915, $M_w$ 7.0; Garfagnana 1920, $M_w$ 6.5; Senigallia 1930, $M_w$ 5.8; Valnerina 1979, $M_w$ 5.8; Colfiorito 1997, $M_w$ 6; L'Aquila 2009, $M_w$ 6.3; Emilia-Romagna 2012, $M_w$ 6; Norcia 2016, $M_w$ 6.5) (Rovida *et al.* 2019).

Several studies provided significant insights about subduction dynamics, magmatism, present-day stress fields, rheology and seismicity (Doglioni *et al.* 1991; Carminati *et al.* 2005; Chiarabba *et al.* 2005; Peccerillo 2005; Riguzzi *et al.* 2012; Montone & Mariucci 2016), fault coupling and fault interaction (Barba *et al.* 2010; Petricca *et al.* 2013; Cheloni *et al.* 2014; Petricca *et al.* 2015; Anderlini *et al.* 2016; Finocchio *et al.* 2016; Mildon *et al.* 2017), coseismic fault dislocation (Atzori *et al.* 2009; Trasatti *et al.* 2011; Tizzani *et al.* 2013; Cesca *et al.* 2017; Cheloni *et al.* 2017; Castaldo *et al.* 2018) and post-seismic relaxation (Cheloni *et al.* 2016; Albano *et al.* 2017; Tung & Masterlark 2018; Albano *et al.* 2019; Pousse-Beltran *et al.* 2020) associated with Italian earthquakes. Few recent studies have successfully simulated the large-scale coupling between long-term geodynamic evolution and short-term seismogenic deformation in northern Italy (D'Acquisto *et al.* 2020; Dal Zilio 2019; Dal Zilio *et al.* 2020) and the role of the brittle-ductile transition on fault reactivation (Carminati & Vadacca 2010; Doglioni *et al.* 2011, 2015, Petricca *et al.* 2018; Petricca *et al.* 2019). Interseismic, coseismic and post-seismic phases have been jointly modelled also for large subduction zones (Savage 1983; Thatcher & Rundle 1984; Matsu'ura & Sato 1989; Wang *et al.* 2012, and references therein). However, a detailed description of the stress, strain and displacement evolution during the interseismic loading, the coseismic dislocation and post-seismic relaxation for normal and reverse fault earthquakes in Italy has not been provided.

In this work, we develop a first-order numerical model to investigate the evolution of interseismic, coseismic and post-seismic stress, strain and displacement fields at the fault scale for typical Italian earthquakes. The model assumes a framework of gravitational and tectonic forces that are compatible with the geodynamics of the Italian territory and is able to simulate the long-term interseismic stress and strain loading, the coseismic brittle episodic dislocation and post-seismic relaxation for normal and reverse fault earthquakes in Italy.

The model consists of three phases. In the interseismic phase, both normal and reverse faults present a locked upper part that simulates an asperity but are unlocked at depth to simulate steady-state creeping under the effect of both lithostatic and tectonic load. In the coseismic phase, the kinematic earthquake dislocation is not generated via forces or displacements applied along the fault edges but is the result of the stress and strain fields inherited from the interseismic phase, accumulated in the volumes adjacent to the fault plane. In the post-seismic phase, stress, strain and displacement variations are modulated by the poroelastic response of the crust to the coseismic dislocation.

The modelling results show evidence of interseismic dilatancy at depth in the proximity of the earthquake hypocentre for extensional earthquakes and volumetric contraction for compressional events. Interseismic stress variation, which is expressed in terms of Coulomb failure stress changes ($\Delta$CFS), highlights the progressive increase of shear stress on the locked fault segments for both normal and reverse fault events. Coseismic fault motion is then triggered by the drop of the hangingwall for extensional events, which recovers the interseismic dilatancy at depth, and by the expulsion of the hangingwall for compressional earthquakes, which is coincident with the instantaneous release of accumulated compressive elastic energy. Finally, in the post-seismic stage, the pore fluid pressure dissipation accommodates further displacements that are consistent with the expected fault kinematics. Our modelling shows that the same forces and boundary conditions can satisfactorily model the interseismic, coseismic and post-seismic data of normal and thrust faults, thus providing a framework that can be used in the study of earthquake physics.

## 2 METHODS

### 2.1 Study area and case studies

The study area (Fig. 1a) encompasses the Central and Northern Apennines and the Po plain. The current geodynamic setting of the area is characterized by the W- and SW-ward subduction of the Adriatic plate, which is E- and NE-ward retreating relative to the upper European plate. This geodynamic setting generates contraction and the generation of the accretionary prism in the frontal part of the belt (southern Po Plain and western Adriatic Sea) and contemporaneous extension in the backarc area all along the Apennines belt and the Tyrrhenian Sea. From the Late Eocene–Oligocene to present time, the Apennines fold-and-thrust belt was characterized by the northeastward (in the Northern Apennines) and eastward (in the Central and Southern Apennines) migration of thrust fronts (Malinverno & Ryan 1986; Patacca *et al.* 1990). To the east, the Adriatic margin served as the foreland to the migrating thrust belt. Starting in the Late Miocene, extensional tectonics, associated with backarc rifting, dissected the Apennines by high-angle normal and oblique faulting, which cut through the pre-existing compressional structures (Hippolyte *et al.* 1994; Ferranti & Oldow 1999) and progressively migrated from the western to the eastern parts of the orogen (Malinverno & Ryan 1986; Patacca *et al.* 1990; Westaway 1990; Doglioni *et al.* 1991; Amato & Montone 1997). The accretionary prism is still active, and thrusting is currently active on the Adriatic side of the Central and Northern Apennines and in the Po plain as indicated by the seismicity, Quaternary sediment deformation and GPS data (Fig. 1a, Cuffaro *et al.* 2010; Livani *et al.* 2018). Thrusting is also active along the Dinarides belts where the Adriatic plate subducts ENE-ward beneath Eurasia and in the eastern Alps, which represents the retrobelt of the Alpine subduction (Fig. 1a), and it is also caused by the northward indentation of the Adriatic plate (Kastelic & Carafa 2012).

In such a geodynamic context, we simulated the stress and strain variations in the interseismic, coseismic and post-seismic phases for three earthquakes that occurred in Italy during the last 15 yr (Fig. 1a). Two earthquakes occurred in the Central Apennines, that is, the 2009 April 6 $M_w$ 6.3 L'Aquila and 2016 October 30 $M_w$ 6.5 Norcia normal-fault earthquakes (hereinafter L'Aquila 2009 and Norcia 2016, respectively), and the third earthquake occurred in the Po plain along the buried front of the Northern Apennines beneath the Po basin, that is, the 2012 May 20 $M_w$ 6.1 Emilia-Romagna reverse-fault event (hereinafter Emilia 2012, Fig. 1a). These events represent remarkable examples of strong Italian earthquakes and mimic the typical seismicity of the area, which is dominated by normal-fault earthquakes along the Apennines belt and reverse-fault earthquakes in the Po plain and Adriatic Sea and characterized by magnitudes ranging between 5.6 and 7 and mean recurrence times between 1000 and 3000 yr (Galli *et al.* 2008).

The L'Aquila 2009 earthquake ($M_w$ 6.3) nucleated approximately 4 km southwest of the city of L'Aquila (Fig. 1b) at a depth of approximately 9 km. The event originated on the Paganica fault, a normal fault dipping 45°–50° to the SW and trending NW-SE (Atzori *et al.* 2009; Falcucci *et al.* 2009; Trasatti *et al.* 2011; Gori *et al.* 2012; Volpe *et al.* 2012; Castaldo *et al.* 2018). The main shock was preceded by a foreshock sequence that lasted for at least 4 months (blue dots in Fig. 1b) and was followed by a 3-yr-long

aftershock sequence that occurred within a 35-km-long NW-SE-trending volume and consisted of more than 90 000 events, including seven $M_w > 5$ events (Chiaraluce *et al.* 2011; Valoroso *et al.* 2013).

The Norcia 2016 earthquake ($M_w$ 6.5) represents the most powerful event registered during a still ongoing (at the time of writing) seismic sequence, which is spread out over the municipalities of Accumoli, Amatrice, Visso and Norcia (Fig. 1c). The sequence started on 2016 August 24 when an $M_w$ 6.0 earthquake nucleated between the towns of Accumuli and Amatrice (Fig. 1c) (Chiaraluce *et al.* 2017; Improta *et al.* 2019). Hundreds of aftershocks were recorded, which gradually migrated away from the earthquake hypocentre, suggesting the possibility of a transient diffusive process (Chiarabba *et al.* 2018; Tung & Masterlark 2018; Albano *et al.* 2019). On 2016 October 30, the Norcia earthquake ($M_w$ 6.5) struck the town of Norcia and caused further damage. According to seismological and geodetic data, the entire sequence activated along a normal fault system striking approximately NW-SE and dipping 40°–55° SW-ward, with a locally listric shape (Cheloni *et al.* 2019, and references therein) and involving a crustal volume of approximately 6000 km³ (Bignami *et al.* 2019). These main faults cross-cut the ground and outcrop along the Mt. Vettore-Bove fault system, which is characterized by extensional/transtensional kinematics and dissects the Meso-Cenozoic clayey/marly and carbonate sedimentary layers of the Central Apennines (Galadini & Galli 2003; Barchi *et al.* 2012). The possible local reactivation of an inherited NW-dipping thrust has been proposed, even if the literature does not consistently agree with this model (Scognamiglio *et al.* 2018; Bonini *et al.* 2019; Cheloni *et al.* 2019; Improta *et al.* 2019).

The Emilia 2012 earthquake ($M_w$ 6.1) occurred on May 20 in the Po Valley. The main shock activated the Ferrara thrust (Fig. 1d), which strikes approximately N140°–150° and dips 20°–40° (Bignami *et al.* 2012; Giuseppe Pezzo *et al.* 2013; Cheloni *et al.* 2016; Livani *et al.* 2018, Fig. 1d) and belongs to the Ferrara salient of the accretionary prism. Following the main event, the rupture propagated eastward and downdip within the Ferrara thrust system (Govoni *et al.* 2014; Scognamiglio *et al.* 2016) and westward along the adjacent Mirandola thrust, where an $M_w$ 5.9 event occurred 9 days later (Fig. 1d). The majority of the aftershocks took place within 3 months of the main shock, and those at $M_w > 5$ occurred within 15 days of the May 20 event (Albano *et al.* 2017).

## 2.2 Conceptual sketch and numerical models

The stress, strain and displacement fields associated with the interseismic, coseismic and post-seismic phases of these events were simulated by assuming a common conceptual scheme. A first-order sketch exhibiting a simple fault plane cross-cutting a medium composed of a brittle upper crust and a plastic deep crust is presented to explain the interseismic, stress and strain accumulation, the coseismic dislocation and the post-seismic relaxation at depth in the hangingwall in extensional and compressional regimes (Doglioni *et al.* 2011; Scholz 2019; Albano *et al.* 2021, Fig. 2).

We speculate that the fault presents two different slip styles along the dip direction, that is, an episodic stick-slip behaviour in the brittle upper part (representing an asperity) and a steady-state shear behaviour in the plastic deep part (Scholz 2019).

In the interseismic phase (Fig. 2a), the gravity force generates a compressive horizontal stress at every depth within the crust. However, the horizontal stress gradually decreases in extensional tectonic settings and progressively increases in compressional tectonic settings (Fig. 2a, Doglioni *et al.* 2011, 2015). Extensional and

compressional regimes generate opposite scenarios. In an extensional tectonic regime, the steady slip of the deep fault segment generates extensional stress and strain gradients, thus developing a dilated volume in the hangingwall above the brittle-plastic transition. Conversely, in a compressional tectonic regime, the inverse slip of the deep fault segment generates compressional stress and strain gradients and develops a contracted volume (Fig. 2a). Since the earth's crust behaves as a medium consisting of a solid skeleton and voids filled with fluids (Fyfe 2012), volume dilation/contraction could involve the development of excess pore fluid pressure in case of the presence at depth of low permeability strata (Lucente *et al.* 2010; Doglioni *et al.* 2014a).

In the coseismic phase, the interseismic stress and strain accumulated in the hangingwall are dissipated (Fig. 2b). In an extensional tectonic regime, the hangingwall instantaneously subsides, thereby recovering the dilated volume at depth. In a compressional tectonic regime, the hangingwall is uplifted, thereby dissipating the accumulated compressional elastic energy in the crustal volume at depth. Since the coseismic dislocation is almost instantaneous, fluid overpressures develop respect to the hydrostatic equilibrium for extensional events in the hangingwall, while fluid underpressures develop for compressional events (Fig. 2b).

In the post-seismic phase (Fig. 2c), the fault plane and the nearby crustal volume accommodate further displacements at a rate that typically decreases with time and whose direction and magnitude depend on the fault mechanism and the physical phenomena acting during the post-seismic relaxation. In the early post-seismic phase, the afterslip and poroelastic stress changes driven by fluid diffusion are the principal driving mechanisms for post-seismic fault relaxation and aftershock nucleation (Govoni *et al.* 2014; Albano *et al.* 2015; Tung & Masterlark 2018; Convertito *et al.* 2020).

This conceptual sketch has been simulated numerically via three 2-D plane-strain models built with the finite-element commercial code MSC Marc 2018 (MSC Software Corporation 2018). The models are oriented approximately SW-NE (sections A, B and C in Fig. 1a) and placed orthogonal to the regional tectonic structures and the strike of the faults that nucleated the earthquakes (Fig. 1, Atzori *et al.* 2009; Pezzo *et al.* 2013; Cheloni *et al.* 2016, 2019).

The complex geology of the study area is simplified into two layers, and the thickness of the top layer varies according to the study case. We adopted a fully coupled, isotropic, linear poroelastic model to describe the evolution of both the stress and strain and pore pressure within the medium (Biot 1941; Rice & Cleary 1976; Wang 2000). The poroelastic constitutive equations that relate the stress, strain, pore pressure and fluid mass content per unit volume are as follows (Segall 2005):

$$2G\,\varepsilon_{ij} = \sigma_{ij} - \frac{\nu}{1+\nu}\sigma_{kk}\delta_{ij} + \frac{(1-2\nu)\,\alpha}{1+\nu}p\delta_{ij} \qquad (1)$$

$$\Delta_m = m - m_0 = \frac{(1-2\nu)\,\alpha\rho_0}{2G\,(1+\nu)}\left[\sigma_{kk} + \frac{3}{B}p\right] \qquad (2)$$

$$q_i = -\rho_0\frac{k}{\eta}\left(\frac{\partial p}{\partial x_i} - \rho_0 g\delta_{ij}\right) \qquad (3)$$

Eq. (1) links the stress and strain in a poroelastic medium, where $\nu$ is the drained Poisson ratio, $G$ is the shear modulus, $p$ is the pore pressure, $\delta_{ij}$ is the Kronecker delta, $\alpha$ is the Biot–Willis coefficient and $\varepsilon_{ij}$ and $\sigma_{ij}$ are the strain and the stress tensor components, respectively.
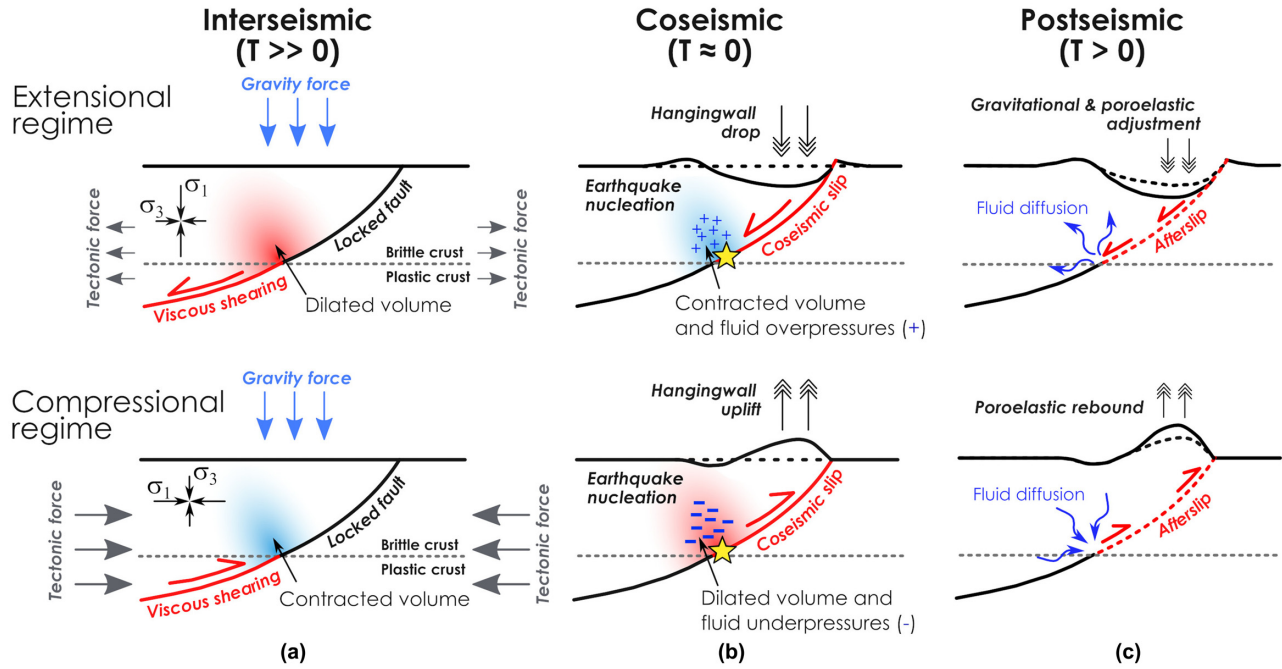
**Figure 2.** First-order conceptual sketch explaining the (a) interseismic, (b) coseismic and (c) post-seismic phases for normal faulting (upper panels) and reverse faulting (lower panels) earthquakes (modified from Doglioni *et al.* 2011, 2015).

Eq. (2) relates the change in fluid mass per unit volume $(\Delta_m)$ to the sum of both the normal stress $(\sigma_{kk})$ and the change in the pore pressure $(p)$, where $m$ is the fluid mass content, $m_0$ is the reference fluid mass content, that is, the product of the fluid density $(\rho_0)$ and the porosity $(n)$, and $B$ is the Skempton coefficient. Eq. (3) is the Darcy's law, where $k$ is the permeability, $g$ is the gravitational acceleration, $q_i$ is the fluid mass flow rate and $\eta$ is the dynamic fluid viscosity. The Skempton (B) and Biot–Willis ($\alpha$) coefficients can be written as follows under the assumption that the solid grains constituting the medium are incompressible (Rice & Cleary 1976; Wang 2000):

$$B = \frac{K_f}{nK + K_f} \tag{4}$$

$$\alpha \cong 1 \tag{5}$$

where $K_f$ and $K$ are the bulk moduli of the pore fluid and the frame, respectively.

Given the first-order nature of the modelling, we adopted average elastic, state and hydraulic parameters for the two layers derived from the literature and geophysical measurements available over the studied areas (Agosta *et al.* 2007; Carannante *et al.* 2013, 2015, Ferraro *et al.* 2020). The assumed values (reported in Table 1) are consistent with those adopted in similar case studies in Italy (Carminati & Vadacca 2010; Albano *et al.* 2015, 2016, Finocchio *et al.* 2016; Castaldo *et al.* 2018). Different elastic parameters do not significantly affect the pattern of the stress and strain field (Doglioni *et al.* 2011). In addition, different hydraulic properties could accelerate or delay the diffusion process, although they have little effect on the general trend and pattern of coseismic and post-seismic pore pressure excess (Doglioni *et al.* 2014a; Albano *et al.* 2017; Albano *et al.* 2019).

One of the most challenging tasks in tectonic modelling is defining the appropriate dimensions and boundary conditions. These were selected according to those proposed by Barba *et al.* (2008,

**Table 1.** Parameters adopted in the numerical analyses.

| Parameter | Description | Layer 1 | Layer 2 |
|---|---|---|---|
| $\rho$ (kg m$^{-3}$) | Mass density | 2600 | |
| $\nu$ | Drained Poisson's ratio | 0.3 | 0.25 |
| $E$ (GPa) | Drained Young's modulus | 18 | 35 |
| $n$ | Porosity | 0.1 | |
| $k$ (m$^2$) | Permeability | $1 \times 10^{-14}$ | |
| $K_f$ (GPa) | Fluid bulk modulus | 2.2 | |
| $\eta$ (Pa·s) | Fluid dynamic viscosity | 0.001 | |
| $\rho_0$ (kg m$^{-3}$) | Fluid density | 1000 | |
| $B$ | Skempton coefficient | 0.75 | 0.61 |

2010) and Finocchio *et al.* (2013, 2016) for the simulation of the interseismic regional tectonic field and by Doglioni *et al.* (2011, 2014a, 2015) for the simulation of interseismic and coseismic phases of both normal and thrust fault earthquakes in Italy.

In detail, the cross-sections extend 220 km horizontally and reach a depth of 40 km. The lower boundary is locked in the vertical direction (Fig. 3), while the upper boundary is free to move. The model's sides feature roller supports that constrain the horizontal movements. This boundary condition agrees with the section-parallel component of the interseismic horizontal velocities from GPS data along sections 1–3 in Fig. 1(a) (Fig. S1, Supporting Information), which show that an approximately zero-velocity area corresponds to the left-hand model boundary of sections 1 and 2 and to both left- and right-hand boundaries of Section 3. To constrain the right-hand sector of the velocity field for sections 1 and 2, which correspond to the Adriatic offshore, we assumed that the Adriatic domain is undergoing compression (Fig. 1a) and established that the horizontal velocity in the middle of the Adriatic offshore area is almost negligible (Carafa *et al.* 2015; Pezzo *et al.* 2020). Thus, we set a point at approximately 80–90 km offshore as a zero-velocity reference, approximately equidistant from the Apennines and Dinarides thrusts (Fig. 1a).
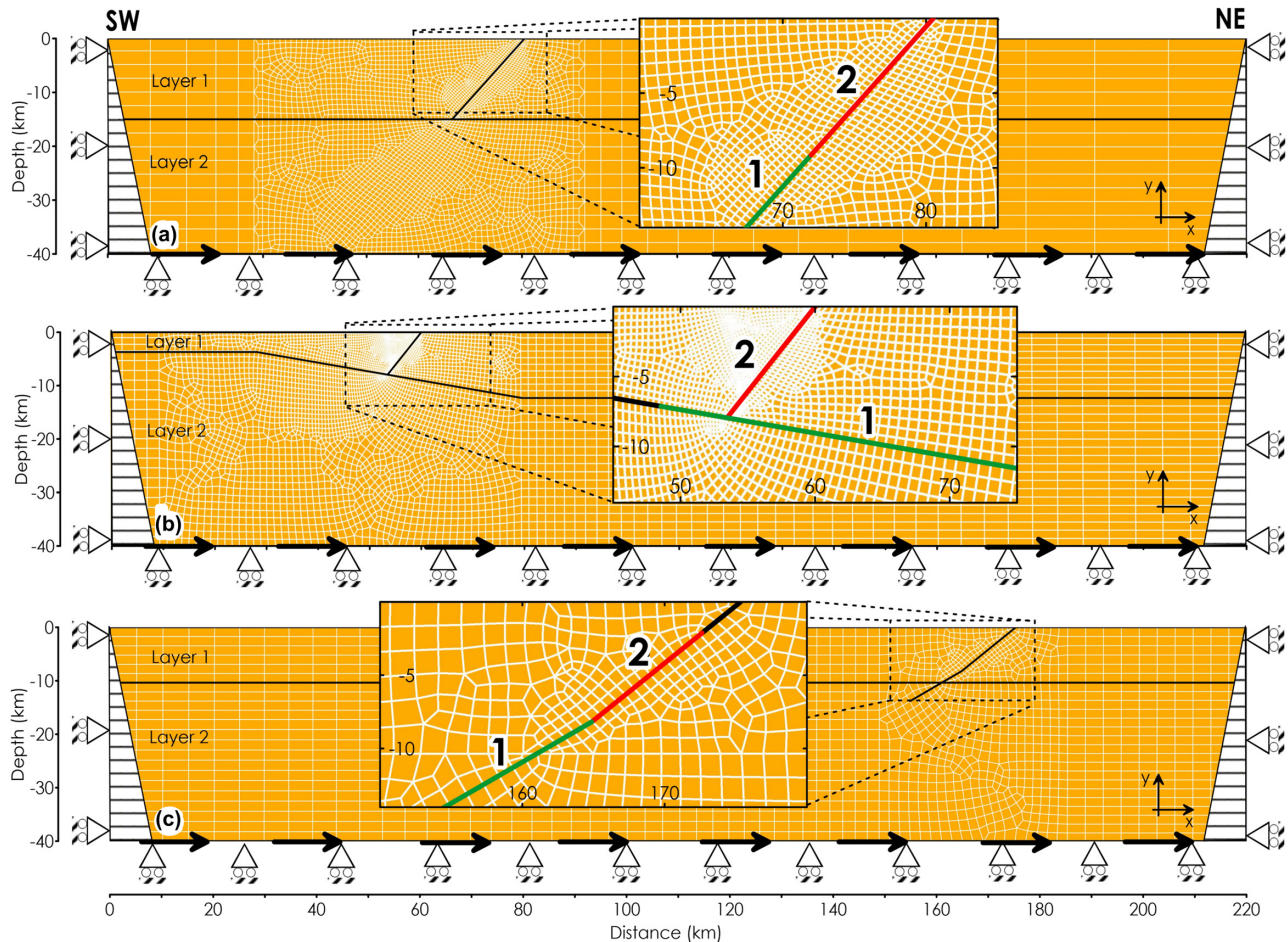
**Figure 3.** Finite-element model geometries and meshes developed for the simulation of the interseismic, coseismic and post-seismic phases associated with the (a) L'Aquila 2009, (b) Norcia 2016 and (c) Emilia 2012 earthquakes.

The applied forces consist of the gravity force, applied as a body force to all of the elements, and shear tractions with constant amplitude applied at the model base (black horizontal arrows in Fig. 3), which are directed towards the NE. The latter simulate the basal shear traction exerted by eastward mantle flow in the Tyrrhenian asthenosphere and the rollback of the Adriatic slab and have been successfully exploited to simulate the active tectonic deformation in the Central Mediterranean (e.g. Barba *et al.* 2008, 2010; Carafa *et al.* 2015). These shear forces are currently implemented in the Shells finite-element code Bird *et al.* (2008), which is widely adopted to simulate plate motion. Basal shear forces, together with the horizontal fixities at the model's sides, have been also successfully employed to model the interseismic deformation and slip rate in Central and Southern Italy (Finocchio *et al.* 2013; Candela *et al.* 2015, 2016) since they enable a first-order description of the ongoing crustal interseismic stretching of the Central and Northern Apennine chain and the compression of the Po plain and the Adriatic offshore (Fig. 1a, Doglioni *et al.* 1999; Carafa & Bird 2016)

Regarding the hydraulic boundary conditions, the lower boundary is assumed to be impermeable, the upper boundary features a fixed fluid pressure equal to the atmospheric pressure, and the sides exhibit hydrostatic pore pressure to simulate a flowing boundary.

The finite-element mesh is composed of eight-node, isoparametric quadrilateral elements with sizes ranging from approximately

0.2 km on the fault segment to 1–5 km at the bottom and sides of the models (Fig. 3).

The faults associated with the L'Aquila 2009, Norcia 2016 and Emilia 2012 events are modelled as frictional contact interfaces (n. 1 and 2 in Fig. 3), where the nodes are doubled so that the footwall and hangingwall slide relative to each other according to the Mohr–Coulomb failure criterion (eq. 6):

$$\tau = (\sigma - p)\,\mu \tag{6}$$

where $\tau$ is the yield shear stress, $\sigma$ is the total normal stress, $p$ is the pore pressure and $\mu$ is the friction coefficient.

In our modelling, the rate and state dependency of friction (Ruina 1983) is not assumed since we are not investigating the processes controlling the timing of rupture; however, we focus on the different stress and strain distributions that develop during the interseismic, coseismic and post-seismic phases (Doglioni *et al.* 2014b), which implies that the fault rupture is assumed a-priori. The two segments composing the fault, that is, segments n. 1 and 2 in Fig. 3, are assumed to be alternatingly locked and unlocked, depending on the simulated phase (Doglioni *et al.* 2011, 2014a). The 'locked' and 'unlocked' status of the fault is achieved by varying the friction coefficient at the interface. In the case of a locked fault, the friction coefficient assumes a large value (i.e., $\approx 0.7$, Byerlee 1978) to avoid the relative movement between the nodes belonging to the footwall and hangingwall. In the case of an unlocked fault, friction is set to a

low value (0.05) (Di Toro *et al.* 2011) to simulate both the viscous sliding of the deep fault segment (n. 1 in Fig. 3) and the coseismic dislocation of the upper fault segment (n. 2 in Fig. 3). Compared with common analytical and numerical approaches (Atzori *et al.* 2009; Anderlini *et al.* 2016; Castaldo *et al.* 2018) no forces or displacements are imposed along the edges of the faults to impose their kinematics. When unlocked, the nodes along the fault's edges move under the effect of the applied far-field boundary conditions, loads and stress distributed within the hangingwall and footwall volumes. Finally, the fluid flow through the fault itself is not considered in the current modelling (Piombo *et al.* 2005; Albano *et al.* 2017; Albano *et al.* 2019).

The geometry of the discontinuities simulating the fault segments are defined on a case-by-case basis according to the available literature. For the L'Aquila 2009 earthquake (Fig. 3a), the fault extent at depth is limited at approximately 14 km because of the presence of a flat-ramp geometry, that is, the Latium–Abruzzo extensional detachment (Lavecchia *et al.* 2017), which delimitates the SW dipping intra-Apennines active faults of Central Italy. The fault dips approximately 47° towards SE (Atzori *et al.* 2009), while the transition between the lower fault segment (segment n.1 in Fig. 3a) and the upper fault segment (n. 2 in Fig. 3a) is located at a depth of approximately 9 km (Doglioni *et al.* 2011) according to the approximate hypocentral depth of the foreshocks that preceded the $M_w$ 6.3 event (Valoroso *et al.* 2013).

For the Norcia 2016 event, the lower fault (n. 1 in Fig. 3b) corresponds to a segment dipping approximately 10° towards the NE. The latter was delineated by the distribution of aftershocks following the Amatrice-Visso-Norcia sequence (Chiaraluce *et al.* 2017; Vuan *et al.* 2017; Improta *et al.* 2019) and probably represents the southeastern extension of the Alto-Tiberina fault. The extent of this fault segment is defined according to the available literature (Boncio & Lavecchia 2000; Carminati *et al.* 2001; Anderlini *et al.* 2016 and references therein, Vadacca *et al.* 2016; Vadacca 2020), while its lower part is uncoupled (i.e., below approximately 4–5 km depth) and steadily creeps during the interseismic phase. The upper fault segment (segment n. 2 in Fig. 3b) dips approximately 48° towards the SW (Cheloni *et al.* 2016; Scognamiglio *et al.* 2018, 2019) and is limited at depth by the segment n. 1 in Fig. 3(b). Any additional synthetic or antithetic fault segments have been neglected since their contribution to earthquake nucleation is secondary (Cheloni *et al.* 2019).

For the Emilia 2012 event, the thrust presents two segments with different dip angles (Fig. 3c), that is, approximately 20° and 40° (Pezzo *et al.* 2013; Livani *et al.* 2018) and is limited in the SW direction by the inner Mirandola thrust (Boccaletti *et al.* 2004; Chiarabba *et al.* 2014). The transition between the upper (segment n. 1 in Fig. 3c) and lower (segment n. 2 in Fig. 3c) portions of the thrust is defined by the lithostratigraphic contact. Indeed, aseismic slip is likely to occur at the contact between the sedimentary succession and the basement while seismogenic slip occurs in Mesozoic carbonate rocks (Bonini *et al.* 2014).

## 2.3 Simulation phases

The simulations include an interseismic, a coseismic and a post-seismic phase. The mechanical and hydraulic boundary conditions are activated at the beginning of the analysis, while the applied forces, locking status of each fault segment, and fluid–solid coupling conditions are specified in Table 2 for each phase.

The interseismic phase is intended to reproduce the stress and strain fields in the crust resulting from the applied boundary conditions and forces. The analysis type is elastic and lasts for one second within a single numerical increment. In this way, we neglect the viscoelastic behaviour of the lower crust and focus on the cumulated interseismic stress and strain field. The interseismic phase is divided into two stages. In the first stage, the model self-consolidates under the gravity force only while assuming that both fault segments (n. 1 and 2 in Table 2 and Fig. 3) are unlocked, which allows the footwall and hangingwall to move with each other and accommodate the lithostatic load. In the second stage, the basal shear tractions (whose magnitude varies on a case-by-case basis) are activated (black arrows in Fig. 3) to simulate the interseismic stretching of the Apennine chain and the contraction in the Po plain and the western Adriatic frontal accretionary prism. In this stage, the deep segment (segment n. 1 in Fig. 3) is unlocked to simulate a fault that experiences steady shear in its lower part while the upper segment (n. 2 in Fig. 3) is locked to simulate a fault asperity during tectonic loading. Pore pressure and stress are fixed to the hydrostatic values and uncoupled to the stress occurring within the hangingwall and footwall volumes; that is, drained conditions are assumed for the fluid phase. Therefore, any poroelastic transients in the interseismic phase are neglected.

The coseismic phase is poroelastic and lasts for one second within a single numerical increment to calculate the undrained coseismic deformation as well as the instantaneous changes in the stress and pore pressure fields induced by unlocking the upper fault segment (n. 2 in Fig. 3) and locking the lower fault segment (n. 1 in Fig. 3). Both the mechanical boundary conditions and the forces applied during the interseismic phase are active in this phase.

The post-seismic phase is poroelastic and spans 2 years to simulate the transient evolution of the stress and pore pressure fields. Viscous effects are neglected in this phase, and the post-seismic stress, strain and displacement field are governed by poroelasticity only. The upper fault segment (n. 2 in Fig. 3) is kept unlocked to simulate further post-seismic slip induced by shear stress changes caused by fluid diffusion. The poroelastic equations are solved every day of the post-seismic period, and they constitute 730 numerical increments required for the solution to converge over the 2-yr interval. The boundary conditions, forces, fault segment status and fluid–solid coupling are the same as those during the coseismic phase.

## 2.4 Model optimization through coseismic deformation

The model's performance was established by performing a trial-and-error procedure to search for the magnitude of the applied shear traction (black arrows in Fig. 3) and the along-dip length of the deep and shallow fault segments (n. 1 and 2 in Fig. 3) that better reproduce the observed coseismic ground displacements. As a reference, we processed the synthetic aperture radar (SAR) data available for each earthquake (for details about the selected SAR data sets, see Table S1, Supporting Information) to show the coseismic ground displacements induced by the main shocks by means of the classic interferometric SAR (InSAR) technique (Massonnet & Feigl 1998) along both the ascending and the descending satellite orbits (Fig. S2, Supporting Information). Details about the SAR data sets, the acquisition dates and the processing scheme are reported in the Supporting Information. The best model is selected by searching for the solution that minimizes the root mean square error (rmse) of the residuals between the observed and modelled coseismic ground

**Table 2.** Applied forces, analysis type, fault locking status and fluid–solid coupling for each modelling phase. For the location of the fault segments, see Fig. 3.

| Modelling phase | Analysis type (period) | Applied forces | Fault segments (L = locked; F = free) n.1 | n.2 | Pore pressure (C = coupled; U = uncoupled) |
|---|---|---|---|---|---|
| Interseismic | Elastic (1 sec) | Gravity force | F | F | U |
|  |  | Basal shear tractions | F | L |  |
| Coseismic | Poroelastic (1 sec) | Gravity + basal shear | L | F | C |
| Post-seismic | Poroelastic (2 years) | Gravity + basal shear | L | F | C |

displacements, which is expressed as follows:

$$\text{rmse} = \sqrt{\frac{1}{N}\sum_{i}^{N}(y_{i,\text{obs}} - y_{i,\text{mod}})^2} \tag{7}$$

where $y_{i,\text{obs}}$ and $y_{i,\text{mod}}$ are the observed and modelled displacements of the $i$th point, respectively, and $N$ is the number of points.

## 3 RESULTS

The results of the numerical simulations refer to the combination of shear traction amplitude and the extent of upper and lower fault segments that best reproduce the coseismic displacement field for the three earthquakes. The effect of varying the amplitude of the basal shear tractions and the along-dip extent of the upper and lower fault segments on the coseismic ground displacements is reported in Fig. S3 in the Supporting Information.

The results are presented in terms of the differential displacement, stress, strain and excess pore pressure ($\Delta p$) in the interseismic, coseismic and post-seismic phases.

### 3.1 Interseismic phase

For an elastic medium, the gravity force produces vertical compressive stress, increasing linearly with depth as a function of the material density and horizontal compressive stress smaller than the vertical one as a function of the Poisson coefficient (Table 1 and Figs S4a and S5a, Supporting Information). The contribution of the topographic load, which has been neglected in our models, does not vary the stress field substantially. Indeed, the spatial distribution of horizontal and vertical stress considering the topographic contribution for the L'Aquila 2009 case study (Figs S4b and S5b, Supporting Information) is similar to that without topography (Figs S4a and S5a, Supporting Information), while the amplitude of horizontal and vertical stress considering topography increases slightly of some tens of MPa in those areas where the topography is high, as observed in Figs S4c and S5c in the Supporting Information.

The applied basal shear tractions, with amplitudes of approximately 1.5, 4 and 1.55 MPa for the L'Aquila 2009, Norcia 2016 and Emilia 2012 events, respectively, modify the horizontal stress and strain field. The left-hand part of the model experiences horizontal stress relaxation and extension (Figs 4a and b, and Figs S6a and b, and S7a and b, Supporting Information), while the right-hand part of the model experiences horizontal stress increase and compression, which is consistent with the extensive tectonic regime of the Central and Northern Apennines and the compressive regime of the

Adriatic Sea offshore and the Po plain (Fig. 1a). The change in horizontal stress induced by the shear forces (Fig. 4a, and Figs S6a and S7a, Supporting Information) is smaller than the horizontal stress induced by the gravity force (Fig. S5, Supporting Information), thus ensuring that the horizontal stress remains always compressive at any point of the model (Bignami *et al.* 2020). The fault segments that simulate the L'Aquila 2009 and Norcia 2016 earthquakes are located in an extensional tectonic field (red line in Figs 4a and b, and Figs S6a and b, Supporting Information), while the fault segment that simulates the Emilia 2012 event falls in a compressional field (Figs S7a and b, Supporting Information).

The tectonic horizontal displacement pattern (Fig. 4c, and Figs S6c and S7c, Supporting Information) is directed towards NE and it is symmetric with respect to the vertical median axis of the model. Displacement is null at the model's sides because of the assumed fixed boundaries and then gradually increases to the maximum at the model's centre.

The computed interseismic horizontal displacements at the ground surface were scaled with respect to time and compared with the GPS-derived interseismic horizontal velocities (Fig. 1a and Fig. S1, Supporting Information) projected along the cross-sections 1 (L'Aquila 2009), 2 (Norcia 2016) and 3 (Emilia 2012) (Fig. 4d, and Figs S6d and S7d, Supporting Information). Different scaling times were selected for the three case studies to reproduce the first-order trend of the interseismic GPS velocities, that is, approximately 1500 yr for the L'Aquila 2009 and Emilia 2012 earthquakes and 4000 yr for the Norcia 2016 event. The comparison shows that the long-wavelength velocity trend of the GPS data (red circles) is well captured by the model (blue curve), which adequately reproduces the NE-directed GPS velocity increase in Central Italy (Fig. 4d and Fig. S6d, Supporting Information) and the almost symmetric velocity increase and decrease in northern Italy (Fig. S7d, Supporting Information).

The assumed interseismic shearing of the deep fault segment (segment n. 1 in Fig. 3) locally modifies the stress and strain fields. For the L'Aquila 2009 and Norcia 2016 normal faulting events, the interseismic displacement pattern and vectors (Figs 5a and b) emphasize the normal dislocation of the fault segment. Both sets of displacements reach their maxima close to the shearing fault segment and gradually decrease moving away from the fault. Such interseismic displacements induce dilation locally at depth in the hangingwall of the locked fault segment (positive volumetric strains in Figs 5d and e), while local volumetric contraction develops in the hangingwall at depths of up to 2 km because of the interseismic ground subsidence caused by the shearing of the deep fault segment. The $\Delta$CFS, calculated on preferential normal planes dipping 47°–48° towards SE (which correspond to the dip of the segment n.2 in
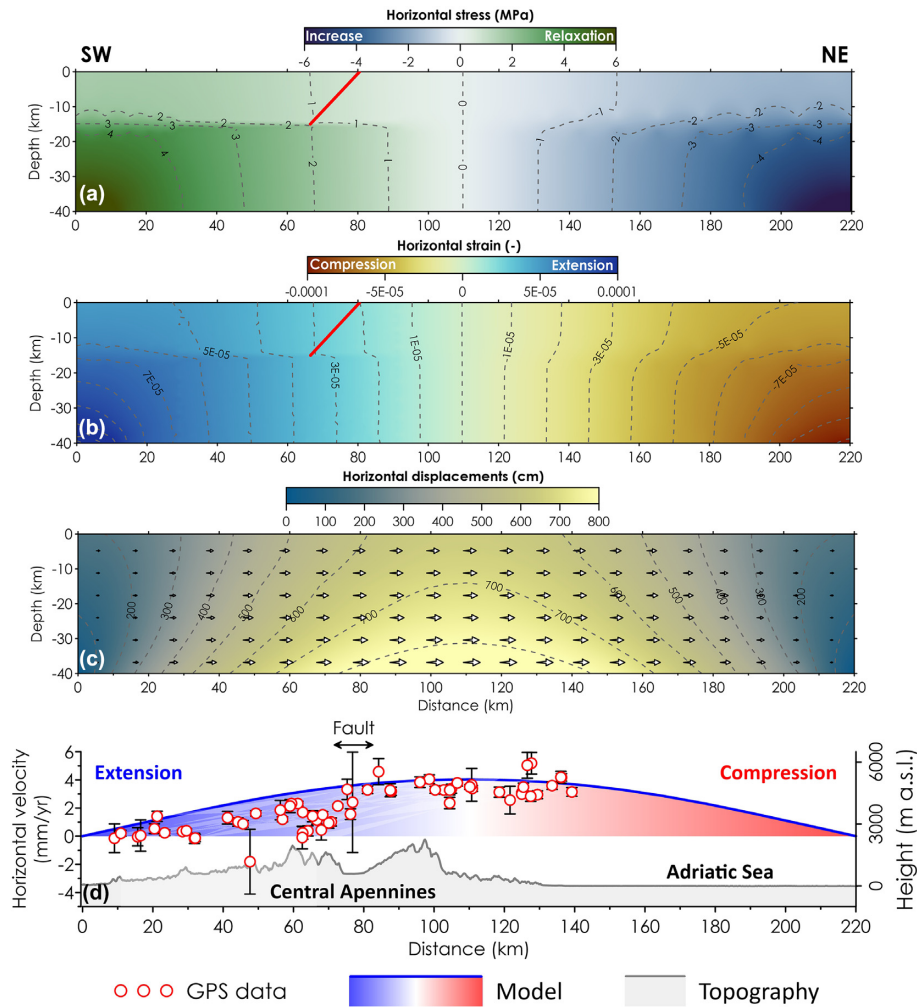
**Figure 4.** Effect of interseismic basal shear only (i.e. without the gravity force) for cross-section 1 of the L'Aquila 2009 earthquake. (a) Differential horizontal stress. The red line identifies the location of the modelled fault segment. (b) Differential horizontal strain. (c) Differential horizontal displacements. (d) Comparison between the modelled interseismic horizontal velocities (blue curve) and those observed with GPS data (red circles) projected along section 1 assuming a distance from the cross-section of 40 km.

Fig. 3) and with $\mu = 0.6$ (Byerlee 1978), show that the locked fault segments fall within a positive $\Delta$CFS area, where normal faulting earthquakes are promoted.

For the Emilia 2012 reverse faulting earthquake, interseismic shearing produces displacements and volumetric strains opposite those obtained for the two normal faulting events. The displacements are oriented mainly upward (Fig. 5c), which causes volumetric contraction (negative values in Fig. 5f) over a wide area of the hangingwall at the transition between the locked and unlocked portions of the fault segment. Conversely, the footwall experiences a general increase of the volumetric strain. The $\Delta$CFS (Fig. 5i) calculated for preferential reverse faulting plane dipping, such as the segment n. 2 in Fig. 3(c), shows that the locked fault segment is located in an area where thrust faulting is promoted.

### 3.2 Coseismic phase

The earthquake dislocations are simulated by unlocking the shallower part of the fault segment (segment n. 2 in Fig. 3). The latter presents an along-dip length of 11.5, 10 and 6 km for the L'Aquila 2009, Norcia 2016 and Emilia 2012 events, respectively.

For the L'Aquila 2009 and Norcia 2016 normal faulting earthquakes, the coseismic deformation patterns (Figs 6a and b) highlight the down left (westward) movement of the hangingwall and the mainly eastward shift of the footwall, which are consistent with geodetic observations and analytical or numerical modelling results (Atzori *et al.* 2009; Cheloni *et al.* 2019). The coseismic dislocation causes the volumetric contraction of the hangingwall at depth (Figs 6d and e), thereby recovering the interseismic volumetric dilation (Figs 5d and e), while dilation occurs in the shallower 1–2 km. The footwall undergoes contraction overall because of the nearly horizontal compression induced by the hangingwall movement. Since pore pressure is coupled with stress, the coseismic volumetric changes induce a $\Delta p$ pattern in excess with respect to the hydrostatic equilibrium (Figs 6g and h). The $\Delta p$ values range nearly $\pm$ 1–2 MPa for the L'Aquila 2009 and Norcia 2016 events. In particular, suprahydrostatic and subhydrostatic pore pressures develop in areas affected by volumetric contraction and dilation, respectively.

For the Emilia 2012 reverse faulting earthquake, the displacement pattern emphasizes the uplift of the hangingwall moving along the thrust plane (Fig. 6c), which causes volumetric dilation in the hangingwall at depth and contraction in the shallower part (Fig. 6f) as
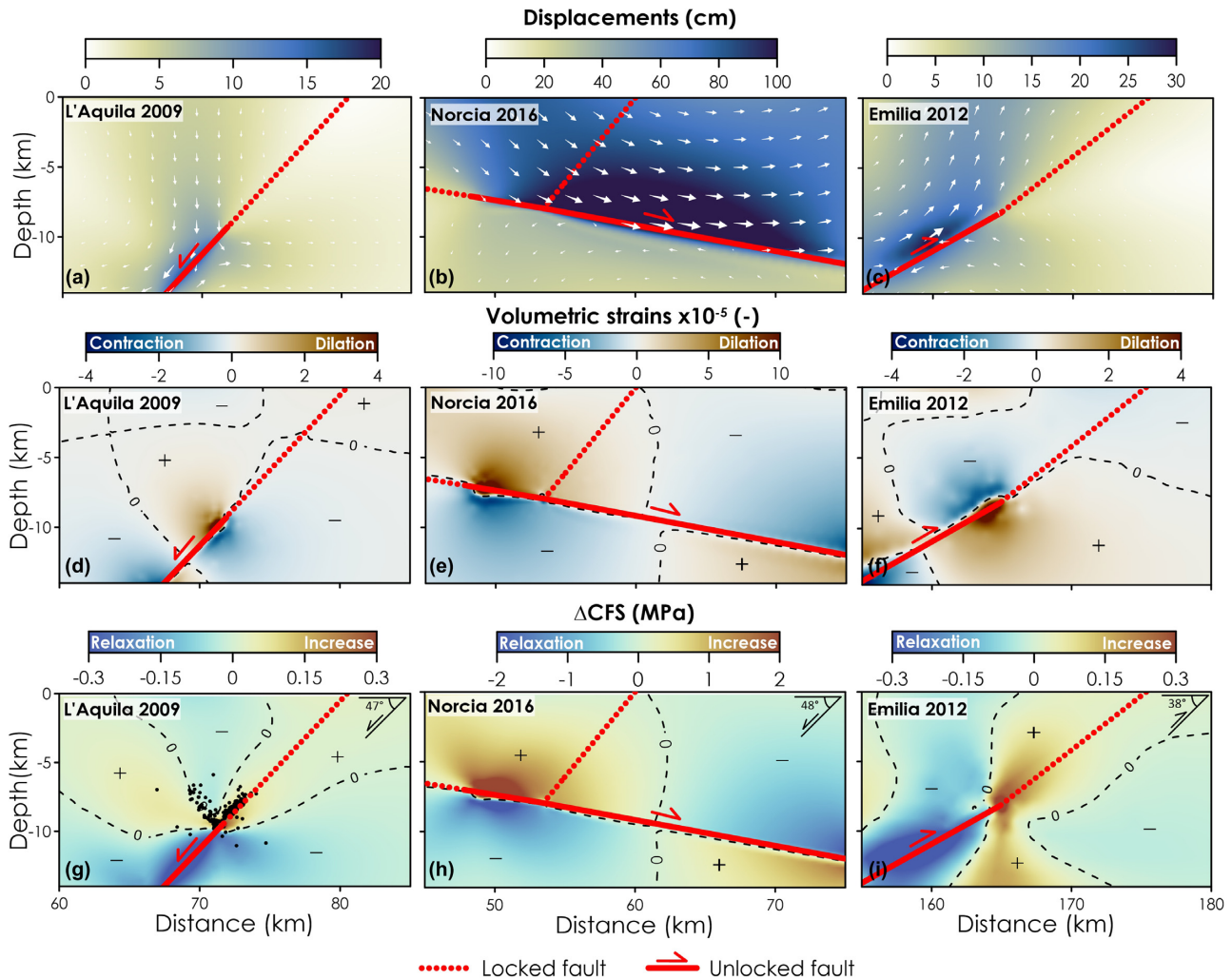
**Figure 5.** Interseismic differential displacements (upper panels), volumetric strain (middle panels), and ΔCFS (lower panels) caused by the interseismic shearing of the deep fault segment only (n. 1 in Fig. 3) calculated for the L'Aquila 2009 (left-hand panels), Norcia 2016 (centre panels) and Emilia 2012 (right-hand panels) events. The black circles in panel (g) identify the hypocentres of the foreshocks registered in the 6 months before the L'Aquila 2009 event (blue dots in Fig. 1b) projected on cross-section 1 in Fig. 1(a).

observed in Doglioni *et al.* (2011). The footwall rather undergoes extension and compression in its upper and lower parts, respectively. The developed $\Delta p$ pattern, which reaches nearly $\pm 1$ MPa at the fault segment, is opposite to the patterns obtained for the normal faulting events because of the different faulting mechanisms (Fig. 6i).

The coseismic displacements are compared with those observed with InSAR (Fig. S2, Supporting Information). The modelled displacement profiles at the ground surface (i.e., at zero depth in Figs 7a–c) for the L'Aquila 2009, Norcia 2016 and Emilia 2012 events are projected along the ascending and descending satellite line of sight (LOS) and compared with the corresponding InSAR observations (Fig. 7). The agreement between the modelled (red line) and measured (blue circles) LOS displacements is satisfactory for both the normal and the reverse faulting events. For the L'Aquila 2009 and Norcia 2016 normal faulting events (Figs 7a and b), the rmses are less than 10 per cent of the maximum observed displacements and comparable to the results of finite-fault dislocation models available in the literature (Atzori *et al.* 2009; Cheloni *et al.* 2016). For the L'Aquila 2009 test case (Fig. 7a), the rmse is

even lower than the uncertainty (i.e. the noise) of the InSAR processing (the error bars in Fig. 7a). For the Norcia 2016 case study, the higher misalignment with respect to InSAR noise is probably due to complexities in the rupture geometry (Cheloni *et al.* 2019), which cannot be modelled with our 2-D approach, and to the high spatial rate of deformation, which can be reflected in unwrapping errors in the InSAR results. For the Emilia 2012 reverse faulting event (Fig. 7c), the rmse is also very low except for the data along the ascending orbit, where the larger misalignment is associated with unwrapping errors caused by the strong loss of coherence in InSAR data.

### 3.3 Post-seismic phase

The coseismic $\Delta p$ values (Figs 6g–i) gradually dissipate during the post-seismic phase because of fluid diffusion. Indeed, 20 days after the simulated earthquakes, the $\Delta p$ peak is approximately 4 times lower than the corresponding coseismic value (Figs 8a–c) because of the ongoing fluid diffusion in the model (grey arrows), which gradually dissipates $\Delta p$. The temporal variation of $\Delta p$ (green
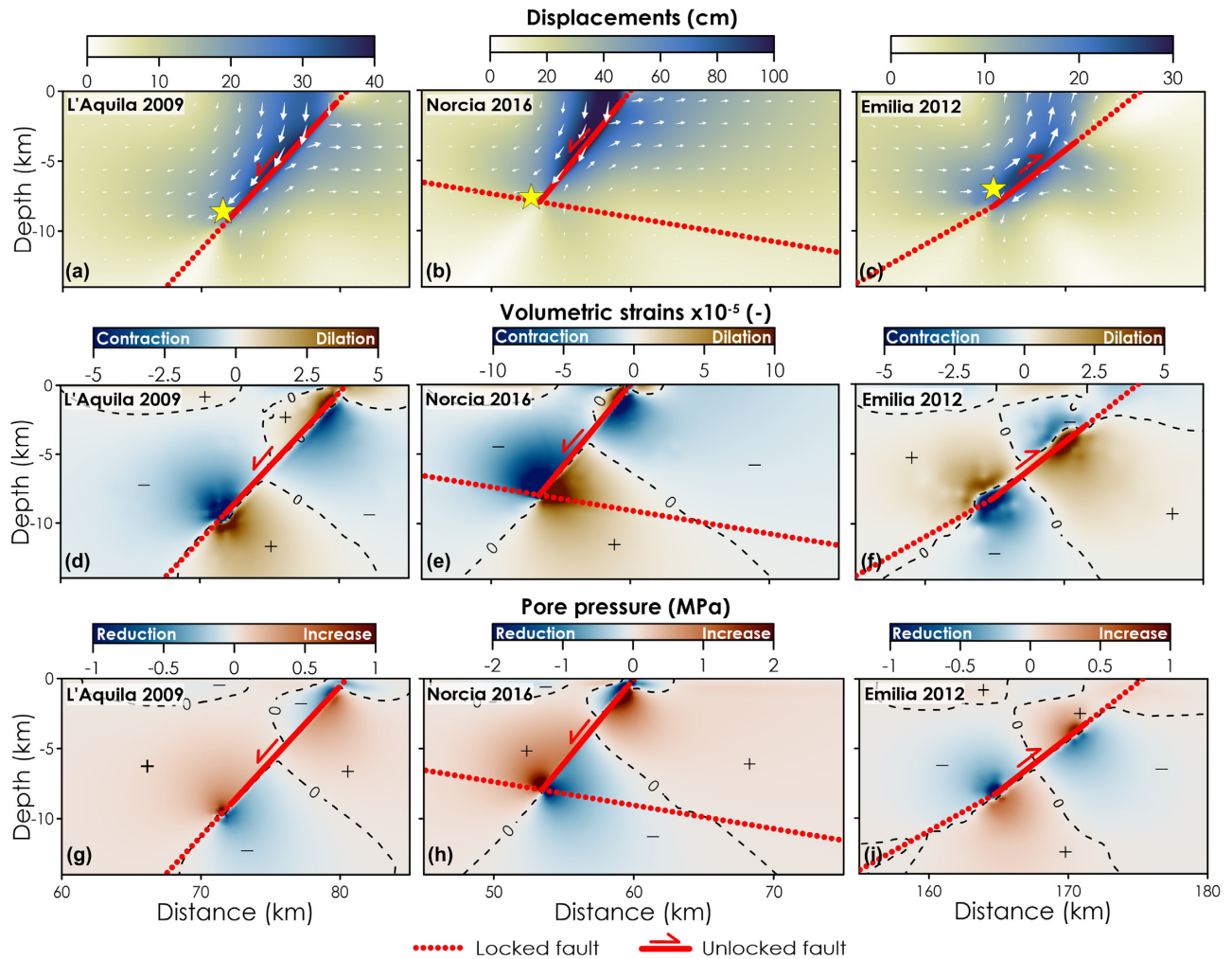
**Figure 6.** Coseismic differential displacements (upper panels), volumetric strain (middle panels) and excess pore pressure with respect to the hydrostatic equilibrium (lower panels) caused by unlocking the shallow fault segment (n. 2 in Fig. 3) calculated for the L'Aquila 2009 (left-hand panels), Norcia 2016 (centre panels) and Emilia 2012 (right-hand panels) earthquakes. The yellow stars in panels (a)–(c) indicate the approximate positions of the main shocks.

curves in Figs 8g–i) at depth in the hangingwall (point 1 in Figs 8a–c) reflects the dissipation of the coseismic suprahydrostatic $\Delta p$ (positive values in Figs 8g and h) and subhydrostatic $\Delta p$ (negative values in Fig. 8i) that develop in the hangingwall for the normal and reverse faulting events, respectively, reaching nearly hydrostatic values (i.e., $\Delta p = 0$ in Figs 8g–i) after approximately one year. It is worth noting that our 2-D approach forces the fluid flow to occur within the modelled sections, thus delaying the time required to dissipate $\Delta p$. With a 3-D model, the dissipation time would be shorter, given the hydraulic properties in Table 1 (Tung & Masterlark 2018).

The progressive dissipation of the coseismic $\Delta p$ alters the effective stress, thus accumulating further strains and deformations at the surface. Indeed, the cumulative post-seismic deformations 2 years after the simulated events show further subsidence of the hangingwall for the L'Aquila 2009 and Norcia 2016 normal faulting earthquakes (Figs 8d and e) and uplift of the hangingwall for the Emilia 2012 reverse faulting earthquake (Fig. 8f). These displacements are due to both the poroelastic contraction/expansion of the medium and the post-seismic slip (i.e. afterslip) of the fault segment (Albano *et al.* 2017). The latter is assumed unlocked during the post-seismic phase (Table 2) and accumulates a mean slip of

approximately 2.5, 7 and 2 cm for the L'Aquila 2009, Norcia 2016 and Emilia 2012 events, respectively.

The temporal variation of the post-seismic displacement (red curves in Figs 8g–i) at the ground level (point 2 in Figs 8g–i) shows a typical exponential decay according to the $\Delta p$ dissipation rate, which is characterized by a rapid increase in displacements in the first few days after the earthquake, reaching an asymptotic value after almost one year. The modelled post-seismic phase is only intended to verify the validity of the assumed boundary conditions and loads. Therefore, the amplitude and rate of post-seismic displacements calculated with our simplified models cannot be directly compared with geodetic observations since they depend on the assumed 2-D plane strain approach and on the assumed mean elastic and hydraulic properties and residual friction along the fault plane, which have been selected from average values derived from the literature and geophysical measurements. Qualitatively, the model correctly predicts post-seismic subsidence for the L'Aquila 2009 and Norcia 2016 events, as observed by D'Agostino *et al.* (2012), Albano *et al.* (2015) and Pousse-Beltran *et al.* (2020), while post-seismic uplift is predicted for the Emilia 2012 event, as observed by Albano *et al.* (2017), thus confirming the effectiveness of the applied boundary conditions and loads.
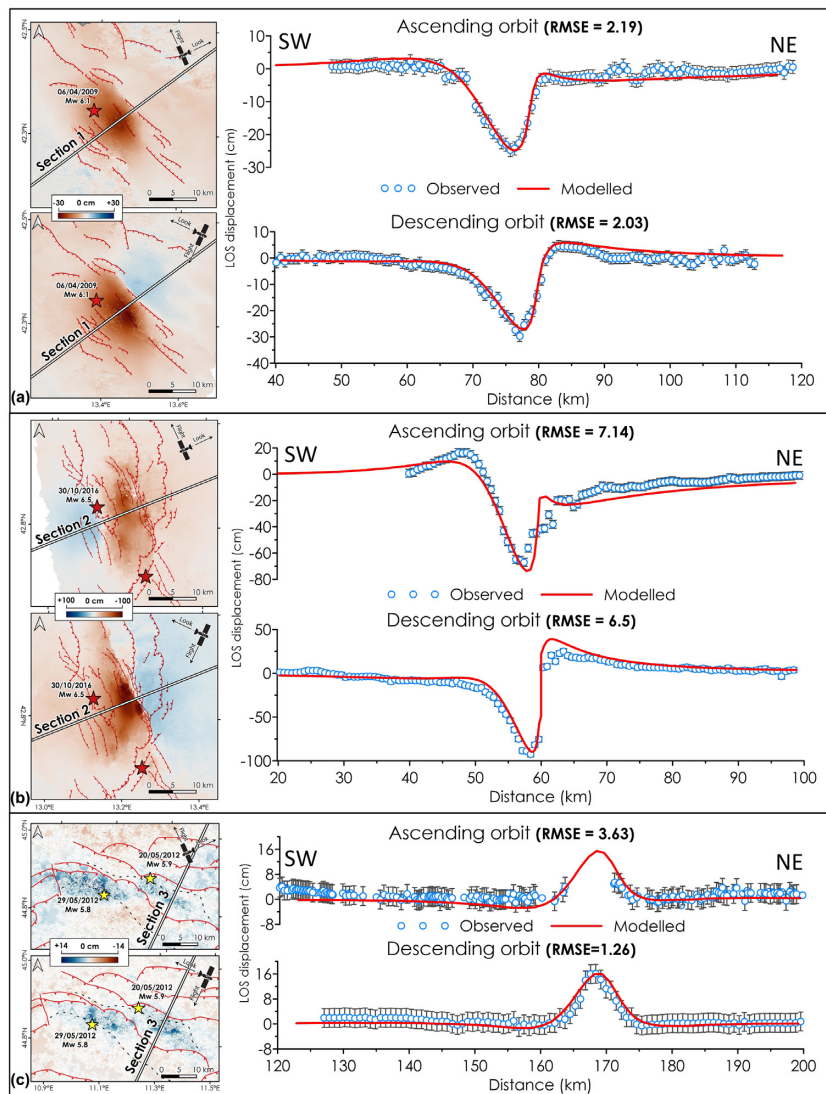
**Figure 7.** Comparison between the observed and modelled LOS displacement profiles along sections 1–3 in Fig. 1(a) for the (a) L'Aquila 2009, (b) Norcia 2016 and (c) Emilia 2012 earthquakes. The vertical bars indicate the uncertainty of the InSAR-derived ground displacements.

## 4 DISCUSSION

The developed numerical model allowed us to reproduce the interseismic loading, coseismic dislocation/unloading and post-seismic relaxation for three normal- and thrust-fault earthquakes in Italy. The imposed boundary conditions, forces and geometrical features, are compatible with the geodynamics of the Italian territory but applicable and valid in other regions characterized by similar conditions (i.e., the occurrence of a brittle shallow crust and a plastic deeper crustal layer). The applied basal shear forces, which simulate the shear traction exerted by eastward mantle flow in the Mediterranean area (Fig. 3), provided a first-order picture of the large-scale crustal interseismic stretching of the Central and Northern Apennines and the ongoing compression of the Adriatic foreland and Po Plain (northern Italy) (Figs 1a and 4, and Figs S6 and S7, Supporting Information, Doglioni *et al.* 1999; Barba *et al.* 2008; Cuffaro *et al.* 2010; Carafa *et al.* 2015). The action of both shear and gravity forces generates a local concentration of stress and strain that, in our case, localizes in the crustal volume at the transition zone between the locked and unlocked fault segments (Fig. 5). Such partitioning

of the interseismic stress and strain promotes the coseismic gravitational lowering of the hangingwall in extensional environments and its elastic expulsion in compressional environments as highlighted by the interseismic increase in ΔCFS for both normal fault and thrust mechanisms (Figs 5g–i).

Regardless of the tectonic style, the interseismic stress and strain pattern is reversed during the coseismic stage: the accumulated differential stress is released, while the dilated volume formed during the interseismic stage for normal faulting is shortened, and vice versa for thrust faulting (Doglioni *et al.* 2011).

Unlocking the brittle segment of the fault generates a sudden drop of the hangingwall for the L'Aquila 2009 and Norcia 2016 events (Figs 6a and b), being the coseismic subsidence carefully recorded by InSAR data (Fig. S2, Supporting Information, Atzori *et al.* 2009; Bignami *et al.* 2019), while the hangingwall is uplifted for the Emilia 2012 event, as observed by InSAR data (Fig. 6c and Fig. S2, Supporting Information, Tizzani *et al.* 2013), thus releasing the stress and strain accumulated during the interseismic phase (Figs 6d–f).
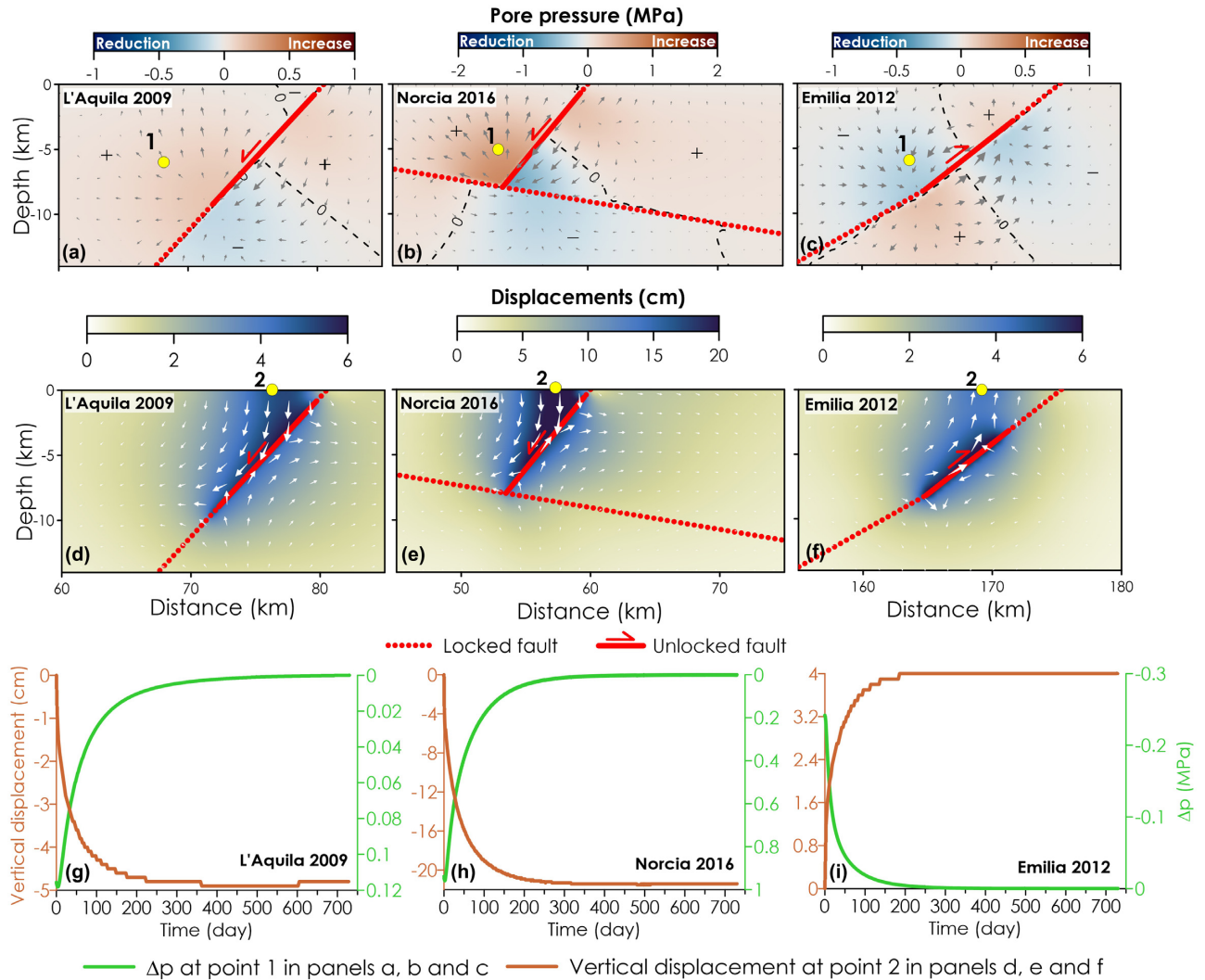
**Figure 8.** Results of the post-seismic phase for the L'Aquila 2009 (left-hand panels), Norcia 2016 (centre panels) and Emilia 2012 (right-hand panels) earthquakes. Upper panels: post-seismic $\Delta p$ pattern respect to the hydrostatic equilibrium 20 days after the simulated earthquakes. The gray arrows identify the pore fluid diffusion direction. Middle panels: cumulative post-seismic displacements two years after the simulated earthquakes. Lower panels: temporal evolution of $\Delta p$ (green curves) at point 1 in panels (a)–(c) and temporal evolution of the vertical displacements (red curves) at point 2 in panels (d)–(f).

Since the model is fully saturated and the pore pressure is coupled with the effective stress, the coseismic slip of the hangingwall alters the crustal pore fluid pressures. Fluids react contrarily when comparing extensional and contractional tectonic settings (Muir-Wood & King 1993; Doglioni *et al.* 2014a; Barberio *et al.* 2017). Indeed, fluids are contained in fractures or primary porosity, and their expulsion and percolation require contraction and dilation, respectively, which are expected at the transition from the interseismic phase to the coseismic stage, when the stress and strain fields invert. This reversal of settings is opposed in sign when comparing contractional and extensional tectonic settings (Figs 6g–i).

In the post-seismic phase, the excess pore pressure triggers fluid flow from regions with suprahydrostatic $\Delta p$, which become further compressed, to regions with subhydrostatic $\Delta p$, which further dilate (Fig. 8). The displacements increase in the post-seismic phase according to the dissipation of the excess pore pressure (Fig. 8) and the poroelastic compression/dilation of the medium. Moreover, fluid diffusion causes the seismogenic fault responsible for the main shock to further slip during the post-seismic phase, thus contributing to the accumulated ground displacements (Albano *et al.* 2017).

Once the post-seismic phase terminates, a new cycle of interseismic loading starts anew.

### 4.1 The role of the basal shear traction

Both the amplitude and the spatial extent of the coseismic displacement field (Fig. 7) depend on the amplitude of the applied basal shear traction and the along-dip length of the upper fault segment (n. 2 in Fig. 3). Indeed, increasing the amplitude of the shear force (Figs S3a–c, Supporting Information) increases the amplitude of the coseismic displacements while increasing the along-dip length of the upper fault segment (Figs S3d and e, Supporting Information) increases both the amplitude and spatial extent of the coseismic displacements.

The earthquake magnitude can increase with the amplitude of basal shear traction for equivalent rupture styles. Indeed, with reference to the two extensional earthquakes, the shear traction for the $M_w$ 6.3 L'Aquila 2009 event ($\cong$1.5 MPa) is approximately 3 times lower than that for the stronger $M_w$ 6.5 Norcia 2016 event ($\cong$4 MPa). The two events occurred along practically the same portion of the

backarc rifting in the central Apennines, which belongs to the upper plate of the Adriatic subduction. The difference in the basal shear force is probably related to geometrical and lithological heterogeneities of the crust, for example, the deep fault segments (n. 1 in Figs 3a and b) of the L'Aquila 2009 and Norcia 2016 events present different dip and orientation. Therefore, the basal shear force can be interpreted as a proxy for the local interseismic loading required to break an asperity that is stronger for the Norcia 2016 event respect to the L'Aquila 2009 earthquake and then to destabilize the more than twice larger brittle crustal volume mobilized during the Norcia 2016 event with respect to the L'Aquila earthquake (Bignami *et al.* 2019).

Interestingly, the amplitude of the basal shear traction required to simulate the coseismic dislocation of the $M_w$ 6.1 Emilia 2012 reverse faulting earthquake is approximately the same as that required for the simulation of the stronger $M_w$ 6.3 L'Aquila 2009 normal faulting earthquake ($\cong$1.5 MPa). This result is not surprising since the gravity force acts in favour of normal faulting events while tends to inhibit reverse faulting events. Therefore, under the same basal shear traction and similar geometrical conditions, the magnitude of a thrust fault event is lower than that of a normal fault event, because the crust moves against or in favour of the gravity force, respectively (Doglioni *et al.* 2014b; Bignami *et al.* 2020). This finding is also consistent with the longer duration and the more numerous aftershocks along normal faults (e.g. Aquila 2009 and Norcia 2016), where the volume moves in favour of the gravity force and does not stop until a final gravitational equilibrium is reached with respect to the compressive settings (e.g. Emilia 2012), which present shorter times and fewer aftershocks because the volume moves against the gravity force (Valerio *et al.* 2017).

The amplitude of the basal traction is model-dependent and cannot be interpreted in absolute terms. None the less, if we assume that the interseismic horizontal stress rate in Central Italy is spatially homogeneous and constant over time, we can analyse the time factor used to scale the modelled interseismic horizontal displacements and fit with the horizontal velocity from GPS data (Fig. 4d, and Figs S6d and S7d, Supporting Information). This time factor could be interpreted as an approximate estimate of the mean recurrence time associated to each event. However, this recurrence time is modelled by a single fault and does not consider the effect of earthquake interaction, which could advance, but also delay, the occurrence of an earthquake on a specific fault segment by several hundred years in Central Italy, according to Wedmore *et al.* 2017. Despite this approximation, a comparison with the available literature shows that the magnitude of the computed time factors resembles to the typical recurrence times for Italian earthquakes. In detail, the scaling factors for the L'Aquila 2009 and Emilia 2012 events, that is, approximately 1500 yr, look like to those estimated for Italian earthquakes with magnitudes ranging between 5.6 and 7.0, that is, approximately 1000–3000 yr. For the Norcia 2016 event, palaeoseismological studies estimated a maximum magnitude of 6.5 and a maximum recurrence time not longer than 4690 yr (Galadini & Galli 2003) for the Mt. Vettore fault. These parameters resemble with both the magnitude of the 2016 October 30 event ($M_w$ 6.5) and the time factor obtained from our model (i.e. approximately 4000 yr).

## 4.2 Model limitations and agreement with the available literature

It is worth discussing the significance of these results in relation to the modelling assumptions and the available literature. The interseismic phase overlooks the long-term, viscous-plastic behaviour of

geomaterials and simulates the accumulation of interseismic stress and strain regardless of time. Together with the assumption of linear elasticity, such an approximation presumes a linear increase in both stress and strain until earthquake occurs. This approach is acceptable since we are interested in investigating the cumulated interseismic stress and strain changes rather than assessing the whole loading path. However, interseismic stress and strain rates are not constant and could change days to months before the earthquake, that is, in the pre-seismic phase (Scholz 2019), thus triggering several phenomena that could be related to the preparatory phase of an earthquake. Examples of such phenomena include modifications of the aseismic ground deformation rate (Moro *et al.* 2017), changes in crustal seismic velocities (Lucente *et al.* 2010), the development of seismicity patterns (Valoroso *et al.* 2013; Bouchon *et al.* 2016) and variations in the hydrological and geochemical properties of fluids (Roeloffs 1988; Thomas 1988). Such interseismic stress and strain rate variations are not considered in our model. However, our first-order results are consistent with field observations. Indeed, the modelled interseismic dilatancy at depth in the hangingwall of extensional settings is compatible with the changes in the $V_p/V_s$ ratio observed several days before the L'Aquila 2009 main shock (Lucente *et al.* 2010), which indicate the presence of fluids and their increase in pressure during the preparation phase. This proves the occurrence of a dilated and multifractured volume in the hangingwall of a normal fault, where fluids may infiltrate and eventually be expelled at the coseismic stage. Moreover, approximately 80 per cent of the foreshocks recorded during the six months before the L'Aquila earthquake (black circles in Fig. 5g) are located in areas where the interseismic $\Delta$CFS increases.

For the Norcia 2016 event, the modelled interseismic shearing of the low-angle normal fault segment (segment n. 1 in Fig. 3b) and the resulting volumetric strain and $\Delta$CFS variations (Figs 5e and h) are compatible with the locations of the seismicity recorded during the six months before the nucleation of the first event of the sequence on 2016 August 24 (Vuan *et al.* 2017). It is worth noting that the maximum stress and strain concentration does not occur at the source fault of the 2016 Norcia earthquake, which depends on the assumed length of the unlocked fault segment in the interseismic phase (n. 1 in Fig. 3b). Such lengths are constrained by literature data (Anderlini *et al.* 2016) and could vary locally.

Our modelling results are consistent with available geodetic measurements. The interseismic phase appropriately simulates the long-wavelength interseismic horizontal ground velocities (Fig. 4d, and Figs S6d and S7d, Supporting Information) from GPS data. However, the model is not able to capture the observed local fluctuations of displacement rates and the horizontal strain rate. This issue is related to the simplified rheological and geometrical approximations imposed in our model and by the assumption of basal shear forces with constant amplitude. In contrast, introducing heterogeneities into both the geometries of the locked/unlocked faults and the modelled geomaterials and assuming non-uniform shear tractions at the model's base improve the observed short-wavelength interseismic strain rates (Finocchio *et al.* 2013, 2016).

The coseismic fault slip style and kinematics are driven by the interseismic crustal stress and strain field resulting from the applied boundary conditions and loads in the far field. This approach, which is different from common analytical modelling techniques (Okada 1985), is able to simulate the observed coseismic scenarios. Indeed, the modelled coseismic displacements for the three case studies effectively reproduce the InSAR observations (Fig. 7). The highlighted discrepancies between the calculated and observed coseismic displacements for the Norcia earthquake (Fig. 7b) are possibly

explained by the occurrence of unmodelled geometrical complexities of the seismogenic fault responsible for the main shock, such as the presence of secondary antithetic faults and inherent 3-D effects that are neglected with our 2-D approach (Cheloni *et al.* 2016; Bonini *et al.* 2019, 2019). The coseismic dislocation of the upper fault segment (segment no. 2 in Fig. 3) is not governed by a self-consistent failure criterion (Ruina 1983; Scholz 2019) but rather is imposed by unlocking the upper fault segment. This simplification is justified by the purpose to investigate the different stress and strain distributions associated with the interseismic, coseismic and post-seismic stages rather than to assess which processes control the timing of rupture.

In our model, the post-seismic evolution of the displacement, stress and strain is governed by poroelasticity only. Different time-dependent physical mechanisms may act at smaller spatial scales or over longer time periods than those accounted for in this work. Assessing the contribution of other physical phenomena to the post-seismic phase is not the goal of this study. Here, we choose to simulate the early post-seismic scenario only, when the probability of strong aftershocks is high and poroelastic effects and afterslip are the controlling phenomena. It is worth noting that afterslip is simulated in our model by assuming the upper fault segment (no. 2 in Fig. 3) unlocked in the post-seismic phase, although it is driven by poroelastic stress and strain changes only.

Although successful in reproducing several aspects of the modelled earthquakes, our 2-D approach suffers from inherent limitations, for example, it neglects motions and fluid diffusion in a direction perpendicular to the modelled cross-section. Such an approximation does not allow us to investigate the stress and strain field at the fault's edges and only permits 2-D pore pressure gradients, thereby delaying the decay of post-seismic pore pressure excess and the accumulation of displacements. Although a 3-D model would certainly produce more accurate results, although the relative importance of the applied boundary conditions and loads would be similar, the first-order results of the 2-D approach are generally valid and provide evidence that has both theoretical and practical implications. In theory, the interseismic differential strain and stress that occur in the crustal volume above the brittle-plastic transition (Fig. 5) could locally involve the development of plastic strain associated with the formation of opposite modes I and II cracks and fractures in the hangingwall of normal and reverse faulting environments where the accumulated interseismic stress is mainly gravitational in extensional tectonic settings ($\sigma_1$ is the lithostatic load), whereas it is elastic in contractional settings ($\sigma_1$ is horizontal and generated by plate convergence). Due to this difference in extensional and compressional tectonic settings, Doglioni *et al.* (2015) proposed the nomenclature of graviquakes and elastoquakes, respectively. Such opposite behaviour of cracks constrains the migration of fluids with opposite sign (Doglioni *et al.* 2014a). Cracks generation and fluids migration have been extensively observed in laboratory fracture experiments and inferred in the field with the observation of crustal velocity anomalies (Lucente *et al.* 2010) associated with changes in void spaces and fluid pressures at depth (Terakawa *et al.* 2010; Scholz 2019, and references therein) preceding and especially contemporaneous to a seismic event. Therefore, a systematic investigation of crustal velocity anomalies at depth in areas where a potential seismogenic fault shows a seismic gap could provide valuable information for predictive purposes. Practically, the findings of our numerical approach, if confirmed, could be implemented in a statistics-based seismicity forecasting technique (Marzocchi *et al.* 2012) to implement a physics-based earthquake forecasting approach that could be worthwhile for the estimation and management of seismic hazard.

# 5 CONCLUSIONS

We contributed to the current understanding of the evolution of stress and strain in the interseismic, coseismic and post-seismic phases associated with a single fault segment by developing a fault-scale numerical model that allowed us to jointly simulate long-term crustal interseismic loading, coseismic brittle episodic dislocation, and post-seismic relaxation for typical normal and reverse faulting earthquakes in Italy based on a single framework of gravitational and tectonic forces.

For the proposed models, the following main conclusions can be drawn.

(i) The assumed gravity and tectonic forces and boundary conditions lead to stress and strain distributions that are compatible with the interseismic ground velocity patterns in central and northern Italy, the coseismic dislocations of normal and reverse faulting earthquakes, and their post-seismic relaxation.

(ii) The strain gradient generated at the brittle-plastic transition during the interseismic phase yields dilation at the base of a locked normal fault, which may be accommodated by the formation of cracks and associated with porosity increase, and contraction at the base of a locked thrust fault, which is associated with crack closure, pressure solution processes and porosity decrease.

(iii) The partitioning of the interseismic stress at the transition between the locked and unlocked fault segments increases the ΔCFS over the locked fault segments and promotes the coseismic subsidence and uplift of the hangingwall in extensional and compressional regimes, respectively.

(iv) The observed post-seismic relaxation (where the model is driven by poroelasticity) shows further ground subsidence and uplift for normal and reverse faulting earthquakes, respectively, which is consistent with the faulting style.

(v) The energy activating the fault is accumulated predominantly in the hangingwall volume. The fault represents the passive plane where the friction during the slip produces the double couple and the related seismic waves. Moreover, the proposed numerical model supports the notion that the main source of energy for normal faulting and thrusting is provided by the lithostatic and classic elastic load, respectively (Doglioni *et al.* 2015).

Our findings provide a possible explanation for the initiation and evolution of an earthquake that could help to develop a physical basis for time-dependent earthquake hazard studies as a function of the tectonic setting.

models expressed in terms of nodal stress, strain and displacement are described in the Supporting Information and are available at the following link: https://zenodo.org/record/3690806#.Xlj6w6hKiHs

# REFERENCES

Agosta, F., Prasad, M. & Aydin, A., 2007. Physical properties of carbonate fault rocks, fucino basin (Central Italy): implications for fault seal in platform carbonates, *Geofluids,* **7,** 19–32.

Albano, M., Barba, S., Bignami, C., Carminati, E., Doglioni, C., Moro, M., Stramondo, S. & Sarolic, M., 2021. Three-dimensional numerical simulation of the interseismic and coseismic phases associated with the 6 April 2009, Mw 6.3 L'Aquila earthquake (Central Italy), *Tectonophysics,* **798,** 228685, doi:10.1016/j.tecto.2020.228685

Albano, M., Barba, S., Saroli, M., Moro, M., Malvarosa, F., Costantini, M., Bignami, C. & Stramondo, S., 2015. Gravity-driven postseismic deformation following the Mw 6.3 2009 L'Aquila (Italy) earthquake, *Sci. Rep.,* **5,** 16558, doi:10.1038/srep16558

Albano, M., Barba, S., Saroli, M., Polcari, M., Bignami, C., Moro, M., Stramondo, S. & Di Bucci, D., 2019. Aftershock rate and pore fluid diffusion: insights from the Amatrice-Visso-Norcia (Italy) 2016 seismic sequence, *J. geophys. Res. Solid Earth,* **124,** 995–1015.

Albano, M., Barba, S., Solaro, G., Pepe, A., Bignami, C., Moro, M., Saroli, M. & Stramondo, S., 2017. Aftershocks, groundwater changes and postseismic ground displacements related to pore pressure gradients: insights from the 2012 Emilia-Romagna earthquake, *J. geophys. Res. Solid Earth,* **122,** 5622–5638.

Albano, M., Saroli, M., Moro, M., Falcucci, E., Gori, S., Stramondo, S., Galadini, F. & Barba, S., 2016. Minor shallow gravitational component on the Mt. Vettore surface ruptures related to Mw 6, 2016 Amatrice earthquake, *Ann. Geophys.,* **59**. doi:10.4401/ag-7299.

Amato, A. & Montone, P., 1997. Present-day stress field and active tectonics in southern peninsular Italy, *Geophys. J. Int.,* **130,** 519–534.

Anderlini, L., Serpelloni, E. & Belardinelli, M.E., 2016. Creep and locking of a low-angle normal fault: insights from the Altotiberina fault in the Northern Apennines (Italy), *Geophys. Res. Lett.,* **43,** 4321–4329.

Atzori, S. *et al.*, 2009. Finite fault inversion of DInSAR coseismic displacement of the 2009 L'Aquila earthquake (central Italy), *Geophys. Res. Lett.,* **36** doi:10.1029/2009GL039293.

Barba, S., Carafa, M.M.C. & Boschi, E., 2008. Experimental evidence for mantle drag in the Mediterranean, *Geophys. Res. Lett.,* **35,** 1–6.

Barba, S., Carafa, M.M.C., Mariucci, M.T., Montone, P. & Pierdominici, S., 2010. Present-day stress-field modelling of southern Italy constrained by stress and GPS data, *Tectonophysics,* **482,** 193–204.

Barberio, M.D., Barbieri, M., Billi, A., Doglioni, C. & Petitta, M., 2017. Hydrogeochemical changes before and during the 2016 Amatrice- Norcia seismic sequence (central Italy), *Sci. Rep.,* 1–12, Springer US. doi:10.1038/s41598-017-11990-8

Barchi, M.R., Alvarez, W. & Shimabukuro, D.H., 2012. The Umbria-Marche Apennines as a double Orogen: observations and hypotheses, *Ital. J. Geosci.,* **131,** 258–271.

Bignami, C., Valerio, E., Carminati, E., Doglioni, C., Petricca, P., Tizzani, P. & Lanari, R., 2020. Are normal fault earthquakes due to elastic rebound or gravitational collapse? *Ann. Geophys.,* **63**. doi:10.4401/ag-8455

Bignami, C., Valerio, E., Carminati, E., Doglioni, C., Tizzani, P. & Lanari, R., 2019. Volume unbalance on the 2016 Amatrice - Norcia (Central Italy) seismic sequence and insights on normal fault earthquake mechanism, *Sci. Rep.,* **9,** 4250, Nature Publishing Group. doi:10.1038/s41598-019-40958-z

Bignami, C. *et al.*, 2012. Coseismic deformation pattern of the Emilia 2012 seismic sequence imaged by Radarsat-1 interferometry, *Ann. Geophys.,* **55,** 789–795.

Biot, M.A., 1941. General theory of three-dimensional consolidation, *J. appl. Phys.,* **12,** 155, doi:10.1063/1.1712886

Bird, P., Liu, Z. & Rucker, W.K.(2008) Stresses that drive the plates from below: Definitions, computational path, model optimization, and error analysis, *Journal of Geophysical Research: Solid Earth,* **113,** B11.

Boccaletti, M. *et al.*, 2004. *Carta Seismo-Tettonica della Regione Emilia-Romagna, scala 1: 250.000 e Note Illustrative*. Selca, Firenze.

Boncio, P. & Lavecchia, G., 2000. A structural model for active extension in Central Italy, *J. Geodyn.,* **29,** 233–244.

Bonini, L., Toscani, G. & Seno, S., 2014. Three-dimensional segmentation and different rupture behavior during the 2012 Emilia seismic sequence (Northern Italy), *Tectonophysics,* **630,** 33–42,

Bonini, L. *et al.*, 2019. Testing different tectonic models for the source of the M w 6.5, 30 October 2016, Norcia Earthquake (Central Italy): a youthful normal fault, or negative inversion of an old thrust? *Tectonics,* **38,** 990–1017.

Bouchon, M., Marsan, D., Durand, V., Campillo, M., Perfettini, H., Madariaga, R. & Gardonio, B., 2016. Potential slab deformation and plunge prior to the Tohoku, Iquique and Maule earthquakes, *Nat. Geosci.,* **9,** 380–383.

Byerlee, J., 1978. Friction of rocks, *Pure appl. Geophys.,* **116,** 615–626.

Candela, S., Mazzoli, S., Megna, A. & Santini, S., 2015. Finite element modelling of stress field perturbations and interseismic crustal deformation in the Val d'Agri region, southern Apennines, Italy, *Tectonophysics,* **657,** 245–259.

Carafa, M.M.C., Barba, S. & Bird, P., 2015. Neotectonics and long-term seismicity in Europe and the Mediterranean region, *J. geophys. Res. Solid Earth,* **120,** 5311–5342.

Carafa, M.M.C. & Bird, P., 2016. Improving deformation models by discounting transient signals in geodetic data: 2. geodetic data, stress directions, and long-term strain rates in Italy, *J. geophys. Res. Solid Earth,* **121,** 5557–5575.

Carannante, S., Argnani, A., Massa, M., D'Alema, E., Lovati, S., Moretti, M., Cattaneo, M. & Augliera, P.(2015) The May 20 (MW 6.1) and 29 (MW 6.0), 2012, Emilia (Po Plain, northern Italy) earthquakes: new seismotectonic implications from subsurface geology and high-quality hypocenter location, *Tectonophysics,* **1234,** 1–17.

Carannante, S., Monachesi, G., Cattaneo, M., Amato, A. & Chiarabba, C., 2013. Deep structure and tectonics of the northern-central Apennines as seen by regional-scale tomography and 3-D located earthquakes, *J. geophys. Res. Solid Earth,* **118,** 5391–5403.

Carminati, E & Doglioni, C., 2012. Alps vs. Apennines: the paradigm of a tectonically asymmetric Earth, *Earth-Sci. Rev.*, **112,** 67–96,

Carminati, E., Doglioni, C. & Barba, S.(2004) Reverse migration of seismicity on thrusts and normal faults *Earth-Science Reviews,* **65,** 3-4, 195–222.

Carminati, E., Lustrino, M. & Doglioni, C., 2012. Geodynamic evolution of the central and western Mediterranean: tectonics vs. igneous petrology constraints, *Tectonophysics,* **579,** 173–192.

Carminati, E., Negredo, A.M., Valera, J.L. & Doglioni, C., 2005. Subduction-related intermediate-depth and deep seismicity in Italy: insights from thermal and rheological modelling, *Phys. Earth planet. Inter.,* **149,** 65–79.

Carminati, E., Toniolo Augier, F. & Barba, S., 2001. Dynamic modelling of stress accumulation in Central Italy: role of structural heterogeneities and rheology, *Geophys. J. Int.,* **144,** 373–390.

Carminati, E. & Vadacca, L., 2010. Two- and three-dimensional numerical simulations of the stress field at the thrust front of the Northern Apennines, Italy, *J. geophys. Res.,* **115,** B12425, doi:10.1029/2010JB007870

Castaldo, R. *et al.*, 2018. Coseismic stress and strain field changes investigation through 3-D finite element modeling of DInSAR and GPS measurements and geological/seismological data: the L'Aquila (Italy) 2009 earthquake case study, *J. geophys. Res. Solid Earth,* **123,** 4193–4222.

Cesca, S. *et al.*, 2017. Complex rupture process of the Mw 7.8, 2016, Kaikoura earthquake, New Zealand, and its aftershock sequence, *Earth planet. Sci. Lett.,* **478,** 110–120.

Cheloni, D., D'Agostino, N. & Selvaggi, G., 2014. Interseismic coupling, seismic potential, and earthquake recurrence on the southern front of the Eastern Alps (NE Italy), *J. geeophys. Res. Solid Earth,* **119,** 4448–4468.

Cheloni, D., Falcucci, E. & Gori, S., 2019. Half-graben rupture geometry of the 30 October 2016 M W 6.6 Mt. Vettore-Mt. Bove Earthquake, Central Italy, *J. geophys. Res. Solid Earth,* **124,** 4091–4118.

Cheloni, D. *et al.*, 2016. New insights into fault activation and stress transfer between en echelon thrusts: the 2012 Emilia, Northern Italy, earthquake sequence, *J. geophys. Res. Solid Earth,* **121,** 4742–4766.

Cheloni, D. *et al.*, 2017. Geodetic model of the 2016 Central Italy earthquake sequence inferred from InSAR and GPS data, *Geophys. Res. Lett.,* **44,** 6778–6787.

Chiarabba, C., De Gori, P., Cattaneo, M., Spallarossa, D. & Segou, M., 2018. Faults geometry and the role of fluids in the 2016–2017 Central Italy seismic sequence, *Geophys. Res. Lett.,* **45,** 6963–6971.

Chiarabba, C., De Gori, P. & Mele, F.M., 2015. Recent seismicity of Italy: active tectonics of the central Mediterranean region and seismicity rate changes after the Mw 6.3 L'Aquila earthquake, *Tectonophysics,* **638,** 82–93.

Chiarabba, C., Jovane, L. & Di Stefano, R., 2005. A new view of Italian seismicity using 20 years of instrumental recordings, *Tectonophysics,* **395,** 251–268, Elsevier. doi:10.1016/j.tecto.2004.09.013

Chiarabba, C. *et al.*, 2014. Frontal compression along the Apennines thrust system: The Emilia 2012 example from seismicity to crustal structure, *J. Geodyn.,* **82,** 98–109.

Chiaraluce, L. *et al.*, 2011. The 2009 L'Aquila (central Italy) seismic sequence, *Boll. di Geofis. Teor. e Appl.,* **52,** 367–387. Retrieved from http://www2.ogs.trieste.it/bgta/provapage.php?id_articolo = 519

Chiaraluce, L. *et al.*, 2017. The 2016 Central Italy seismic sequence: a first look at the mainshocks, aftershocks, and source models, *Seismol. Res. Lett.,* **88,** 757–771.

Convertito, V., De Matteis, R., Improta, L. & Pino, N.A., 2020. Fluid-triggered aftershocks in an anisotropic hydraulic conductivity geological complex: the case of the 2016 Amatrice Sequence, Italy, *Front. Earth Sci.,* **8**. doi:10.3389/feart.2020.541323

Crameri, F., 2018. Scientific colour-maps. doi:10.5281/ZENODO.1287763

Crameri, F., Shephard, G.E. & Heron, P.J., 2020. The misuse of colour in science communication, *Nat. Commun.,* **11,** 5444, doi:10.1038/s41467-020-19160-7

Cuffaro, M., Riguzzi, F., Scrocca, D., Antonioli, F., Carminati, E., Livani, M. & Doglioni, C., 2010. On the geodynamics of the northern Adriatic plate, *Rend. LINCEI,* **21,** 253–279.

D'Acquisto, M., Dal Zilio, L., Molinari, I., Kissling, E., Gerya, T. & Dinther, Y. van., 2020. Tectonics and seismicity in the Northern Apennines driven by slab retreat and lithospheric delamination, *Tectonophysics,* **789,** 228481, doi:10.1016/j.tecto.2020.228481

D'Agostino, N., Cheloni, D., Fornaro, G., Giuliani, R. & Reale, D.(2012) Space-time distribution of afterslip following the 2009 L'Aquila earthquake *Journal of Geophysical Research: Solid Earth,* **117,** B12.

Dal Zilio, L., 2019. *Cross-scale modeling of mountain building and the seismic cycle: From Alps to Himalaya,* ETH Zurich, Zurich, p. 196, doi:10.3929/ethz-b-000377255.

Dal Zilio, L., Kissling, E., Gerya, T. & Van Dinther, Y.(2020) Slab Rollback Orogeny Model: A Test of Concept, *Geophysical Research Letters,* **47,** 18, doi:10.1029/2020GL089917

Devoti, R. *et al.*, 2017. A combined velocity field of the Mediterranean region, *Ann. Geophys.,* **60,** S0215. doi:10.4401/ag-7059

Di Toro, G. *et al.*, 2011. Fault lubrication during earthquakes, *Nature,* **471,** 494–498, doi:10.1038/nature09838

Doglioni, C., Barba, S., Carminati, E. & Riguzzi, F., 2011. Role of the brittle-ductile transition on fault activation, *Phys. Earth planet. Inter.,* **184,** 160–171.

Doglioni, C., Barba, S., Carminati, E. & Riguzzi, F., 2014a. Fault on–off versus coseismic fluids reaction, *Geosci. Front.,* **5,** 767–780,

Doglioni, C., Barba, S., Carminati, E. & Riguzzi, F., 2014b. Fault on-off versus strain rate and earthquakes energy, *Geosci. Front.,* **6,** 265–276.

Doglioni, C., Carminati, E., Cuffaro, M. & Scrocca, D.(2007) Subduction kinematics and dynamic constraints *Earth-Science Reviews,* **83,** 3-4, 125–175.

Doglioni, C., Carminati, E., Petricca, P. & Riguzzi, F., 2015. Normal fault earthquakes or graviquakes, *Sci. Rep.,* **5,** 12110. doi:10.1038/srep12110

Doglioni, C., Gueguen, E., Harabaglia, P. & Mongelli, F., 1999. On the origin of west-directed subduction zones and applications to the western Mediterranean, *Geol. Soc. Spec. Publ.,* **156,** 541–561.

Doglioni, C., Moretti, I. & Roure, F., 1991. Basal lithospheric detachment, eastward mantle flow and mediterranean geodynamics: a discussion, *J. Geodyn.,* **13,** 47–65, doi:10.1016/0264-3707(91)90029-E

Falcucci, E. *et al.*, 2009. The Paganica fault and surface coseismic ruptures caused by the 6 April 2009 Earthquake (L'Aquila, Central Italy), *Seismol. Res. Lett.,* **80,** 940–950.

Ferranti, L. & Oldow, J.S., 1999. History and tectonic implications of low-angle detachment faults and orogen parallel extension, Picentini Mountains, Southern Apennines fold and thrust belt, Italy, *Tectonics,* **18,** 498–526.

Ferraro, F., Agosta, F., Prasad, M., Vinciguerra, S., Violay, M. & Giorgioni, M., 2020. Pore space properties in carbonate fault rocks of peninsular Italy, *J. Struct. Geol.,* **130,** 103913, doi:10.1016/j.jsg.2019.103913

Finocchio, D., Barba, S. & Basili, R., 2016. Slip rate depth distribution for active faults in Central Italy using numerical models, *Tectonophysics,* **687,** 232–244.

Finocchio, D., Barba, S., Santini, S. & Megna, A., 2013. Interpreting the interseismic deformation of the Altotiberina fault (central Italy) through 2D modelling, *Ann. Geophys.,* **56**. doi:10.4401/ag-5806

Fyfe, W.S., 2012. *Fluids in the Earth's Crust: Their Significance In Metamorphic, Tectonic And Chemical Transport Process*. Developments in Geochemistry, Elsevier Science.

Galadini, F. & Galli, P., 2003. Paleoseismology of silent faults in the central Apennines (Italy): the Mt. Vettore and Laga Mts. Faults, *Ann. Geophys.,* **46,** 815–836.

Galli, P., Galadini, F. & Pantosti, D., 2008. Twenty years of paleoseismology in Italy, *Earth-Sci. Rev.,* **88,** 89–117.

Gori, S. *et al.*, 2012. Constraining primary surface rupture length along the Paganica fault (2009 L'Aquila earthquake) with geological and geodetic (DInSAR and GPS) data, *Ital. J. Geosci.,* **131,** 359–372.

Govoni, A. *et al.*, 2014. The 2012 Emilia seismic sequence (Northern Italy): imaging the thrust fault system by accurate aftershock location, *Tectonophysics,* **622,** 44–55.

Hippolyte, J.C., Angelier, J. & Roure, F., 1994. A major geodynamic change revealed by Quaternary stress patterns in the southern Apennines (Italy), *Tectonophysics,* **230,** 199–210.

Improta, L. *et al.*, 2019. Multi-segment rupture of the 2016 Amatrice-Visso-Norcia seismic sequence (central Italy) constrained by the first high-quality catalog of Early Aftershocks, *Sci. Rep.,* **9,** 6921, doi:10.1038/s41598-019-43393-2

Kastelic, V. & Carafa, M.M.C., 2012. Fault slip rates for the active External Dinarides thrust-and-fold belt, *Tectonics,* **31,** doi:10.1029/2011TC003022

Lavecchia, G. *et al.*, 2017. Multidisciplinary inferences on a newly recognized active east-dipping extensional system in Central Italy, *Terra Nova,* **29,** 77–89,

Livani, M., Scrocca, D., Arecco, P. & Doglioni, C., 2018. Structural and stratigraphic control on salient and recess development along a thrust belt front: the Northern Apennines (Po Plain, Italy), *J. geophys. Res. Solid Earth,* **123,** 4360–4387.

Lucente, F.P., De Gori, P., Margheriti, L., Piccinini, D., Di Bona, M., Chiarabba, C. & Piana Agostinetti, N., 2010. Temporal variation of seismic velocity and anisotropy before the 2009 M W 6.3 L'Aquila earthquake, Italy, *Geology,* **38,** 1015–1018.

Malinverno, A. & Ryan, W.B.F., 1986. Extension in the Tyrrhenian Sea and shortening in the Apennines as result of arc migration driven by sinking of the lithosphere, *Tectonics,* **5,** 227–245.

Marzocchi, W., Douglas Zechar, J. & Jordan, T.H., 2012. Bayesian forecast evaluation and ensemble earthquake forecasting, *Bull. seism. Soc. Am.,* **102,** 2574–2584.

Massonnet, D. & Feigl, K.L., 1998. Radar interferometry and its application to changes in the Earth's surface, *Rev. Geophys.,* **36,** 441–500.

Matsu'ura, M. & Sato, T., 1989. A dislocation model for the earthquake cycle at convergent plate boundaries, *Geophys. J. Int.,* **96,** 23–32.

Meletti, C., Patacca, E. & Scandone, P., 2000. Construction of a seismotectonic model: the case of Italy, *Pure appl. Geophys.,* **157,** 11–35,

Mildon, Z.K., Roberts, G.P., Faure Walker, J.P. & Iezzi, F., 2017. Coulomb stress transfer and fault interaction over millennia on non-planar active

normal faults: the Mw 6.5–5.0 seismic sequence of 2016–2017, central Italy, *Geophys. J. Int.,* **210**, 1206–1218.

Montone, P. & Mariucci, M.T., 2016. The new release of the Italian contemporary stress map, *Geophys. J. Int.,* **205**, 1525–1531.

Moro, M. *et al.*, 2017. New insights into earthquake precursors from InSAR, *Sci. Rep.,* **7**, 12035, doi:10.1038/s41598-017-12058-3

MSC Software Corporation, 2018. Marc 2018.1 Volume A: Theory and User Information. Retrieved March 16, 2018. Available at: http://www.mscsoftware.com/it/product/marc

Muir-Wood, R. & King, G.C.P., 1993. Hydrological signatures of earthquake strain, *J. geophys. Res.,* **98**. doi:10.1029/93jb02219

Okada, Y., 1985. Surface deformation due to shear and tensile faults in a half-space, *Bull. seism. Soc. Am.,* **75**, 1135–1154.

Palano, M., 2015. On the present-day crustal stress, strain-rate fields and mantle anisotropy pattern of Italy, *Geophys. J. Int.,* **200**, 969–985.

Patacca, E., Sartori, R. & Scandone, P., 1990. Tyrrhenian basin and Apenninic arcs: kinematic relations since Late Tortonian times, *Mem. della Soc. Geol. Ital.,* **45**, 425–451.

Patacca, E. & Scandone, P., 2001. Late thrust propagation and sedimentary response in the thrust-belt—foredeep system of the Southern Apennines (Pliocene-Pleistocene), in *Anatomy of an Orogen: the Apennines and Adjacent Mediterranean Basins,* pp. 401–440, Springer, Netherlands.

Peccerillo, A., 2005. *Plio-Quaternary Magmatism in Italy,* Springer-Verlag.

Petricca, P., Barba, S., Carminati, E., Doglioni, C. & Riguzzi, F., 2015. Graviquakes in Italy, *Tectonophysics,* **656**, 202–214.

Petricca, P., Carafa, M.M.C., Barba, S. & Carminati, E., 2013. Local, regional, and plate scale sources for the stress field in the Adriatic and Periadriatic region, *Mar. Pet. Geol.,* **42**, 160–181.

Petricca, P., Carminati, E. & Doglioni, C., 2019. The decollement depth of active thrust faults in Italy: implications on potential earthquake magnitude, *Tectonics,* **38**, 3990–4009.

Petricca, P., Carminati, E., Doglioni, C. & Riguzzi, F., 2018. Brittle-ductile transition depth versus convergence rate in shallow crustal thrust faults: considerations on seismogenic volume and impact on seismicity, *Phys. Earth planet. Inter.,* **284**, 72–81.

Pezzo, G. *et al.*, 2013. Coseismic deformation and source modeling of the May 2012 Emilia (Northern Italy) earthquakes, *Seismol. Res. Lett.,* **84**, 645–655.

Pezzo, G. *et al.*, 2020. Active fold-thrust belt to foreland transition in northern adria, italy, tracked by seismic reflection profiles and GPS offshore data, *Tectonics,* **39**, doi:10.1029/2020TC006425

Piombo, A., Martinelli, G. & Dragoni, M., 2005. Post-seismic fluid flow and Coulomb stress changes in a poroelastic medium, *Geophys. J. Int.,* **162**, 507–515.

Pousse-Beltran, L., Socquet, A., Benedetti, L., Doin, M., Rizza, M. & D'Agostino, N., 2020. Localized afterslip at geometrical complexities revealed by InSAR After the 2016 Central Italy seismic sequence, *J. geophys. Res. Solid Earth,* **125**, doi:10.1029/2019JB019065

Rice, J.R. & Cleary, M.P., 1976. Some basic stress-diffusion solutions for fluid saturated elastic porous media with compressible constituents, *Rev. Geophys. Sp. Phys.,* **14**, 227–241, doi:10.1029/RG014i002p00227

Riguzzi, F., Crespi, M., Devoti, R., Doglioni, C., Pietrantonio, G. & Pisani, A.R., 2012. Geodetic strain rate and earthquake size: new clues for seismic hazard studies, *Phys. Earth planet. Inter.,* **206–207**, 67–75,

Roeloffs, E.A., 1988. Hydrologic precursors to earthquakes: a review, *Pure appl. Geophys.,* **126**, 177–209,

Rovida, A., Locati, M., Camassi, R., Lolli, B. & Gasperini, P., 2019. Catalogo Parametrico dei Terremoti Italiani (CPTI15), versione 2.0, doi:10.6092/INGV.IT-CPTI15

Ruina, A., 1983. Slip instability and state variable friction laws, *J. geophys. Res. Solid Earth,* **88**, 10359–10370.

Savage, J.C., 1983. A dislocation model of strain accumulation and release at a subduction zone, *J. geophys. Res.,* **88**, 4984–4996.

Scholz, C.H., 2019. *The Mechanics of Earthquakes and Faulting,* Cambridge University Press. doi:10.1017/9781316681473

Scognamiglio, L., Magnoni, F., Tinti, E. & Casarotti, E., 2016. Uncertainty estimations for moment tensor inversions: the issue of the 2012 May 20 Emilia earthquake, *Geophys. J. Int.,* **206**, 792–806.

Scognamiglio, L. *et al.*, 2018. Complex fault geometry and rupture dynamics of the M W 6.5, 30 October 2016, Central Italy earthquake, *J. geophys. Res. Solid Earth,* **123**, 2943–2964.

Segall, P., 2005. *Earthquake and Volcano Deformation,* Hoboken, NJ, USA: John Wiley & Sons, Inc.

Terakawa, T., Zoporowski, A., Galvan, B. & Miller, S.A., 2010. High-pressure fluid at hypocentral depths in the L'Aquila region inferred from earthquake focal mechanisms, *Geology,* **38**, 995–998.

Thatcher, W. & Rundle, J.B., 1984. A viscoelastic coupling model for the cyclic deformation due to periodically repeated earthquakes at subduction zones, *J. geophys. Res.,* **89**, 7631–7640,

Thomas, D., 1988. Geochemical precursors to seismic activity, *Pure appl. Geophys.,* **126**, 241–266.

Tizzani, P. *et al.*, 2013. New insights into the 2012 Emilia (Italy) seismic sequence through advanced numerical modeling of ground deformation InSAR measurements, *Geophys. Res. Lett.,* **40**, 1971–1977.

Trasatti, E., Kyriakopoulos, C. & Chini, M., 2011. Finite element inversion of DInSAR data from the Mw 6.3 L'Aquila earthquake, 2009 (Italy), *Geophys. Res. Lett.,* **38**, n/a–n/a, doi:10.1029/2011GL046714

Tung, S. & Masterlark, T., 2018. Delayed Poroelastic Triggering of the 2016 October Visso Earthquake by the August Amatrice Earthquake, Italy, *Geophys. Res. Lett.,* **45**, 2221–2229.

Vadacca, L., 2020. The altotiberina low-angle normal fault (Italy) can fail in moderate-magnitude earthquakes as a result of stress transfer from stable creeping fault area, *Geosciences,* **10**, 144.

Vadacca, L., Casarotti, E., Chiaraluce, L. & Cocco, M., 2016. On the mechanical behaviour of a low-angle normal fault: the Alto Tiberina fault (Northern Apennines, Italy) system case study, *Solid Earth,* **7**, 1537–1549,

Valerio, E., Tizzani, P., Carminati, E. & Doglioni, C., 2017. Longer aftershocks duration in extensional tectonic settings, *Sci. Rep.,* **7**, 1–12,

Valoroso, L., Chiaraluce, L., Piccinini, D., Di Stefano, R., Schaff, D. & Waldhauser, F., 2013. Radiography of a normal fault system by 64,000 high-precision earthquake locations: the 2009 L'Aquila (central Italy) case study, *J. geophys. Res. Solid Earth,* **118**, 1156–1176.

Volpe, M., Piersanti, A. & Melini, D., 2012. Complex 3-D Finite element modelling of the 2009 April 6 L'Aquila earthquake by inverse analysis of static deformation, *Geophys. J. Int.,* **188**, 1339–1358.

Vuan, A., Sugan, M., Chiaraluce, L. & Di Stefano, R., 2017. Loading rate variations along a midcrustal shear zone preceding the Mw6.0 earthquake of 24 August 2016 in Central Italy, *Geophys. Res. Lett.,* **44**, 12 170–112 180.

Wang, H., 2000. *Theory of Linear Poroelasticity with Applications to Geomechanics and Hydrogeology,* Princeton University Press.

Wang, K., Hu, Y. & He, J., 2012. Deformation cycles of subduction earthquakes in a viscoelastic Earth, *Nature,* **484**, 327–332.

Wedmore, L. N. J., Faure Walker, J. P., Roberts, G. P., Sammonds, P. R., McCaffrey, K. J. W. & Cowie, P. A.(2017) A 667 year record of coseismic and interseismic Coulomb stress changes in central Italy reveals the role of fault interaction in controlling irregular earthquake recurrence intervals *Journal of Geophysical Research: Solid Earth,* **122**, 7, 5691–5711.

Westaway, R., 1990. Block rotation in western Turkey 1. Observational evidence, *J. geophys. Res.,* **95**, 19857–19884.

## SUPPORTING INFORMATION

Supplementary data are available at *GJI* online.

**Table S1.** Main parameters of the exploited SAR data sets.
**Figure S1.** Interseismic horizontal displacement field from GPS data. (a) Interseismic horizontal velocities at GPS sites with respect to a fixed Eurasian frame (with 95 per cent error ellipses; for information about the GPS processing, refer to Devoti *et al.* 2017) with the locations of the investigated earthquakes and the modelled cross-sections. (b) Horizontal GPS velocities projected along section 1 in panel (a). (c) Horizontal GPS velocities projected along section 2 in panel (a). (d) Horizontal GPS velocities projected along section 3 in

panel (a). A distance of 40 km from the sides of the cross sections has been assumed for the projection of the horizontal velocities. The red curve represents a third-order interpolation function of the GPS velocities. (d) Scheme of the 2-D modelled cross-sections in Fig. 3 with the location of the fault segments associated with the L'Aquila 2009, Norcia 2016 and Emilia 2012 earthquakes.

**Figure S2.** Coseismic ground displacement fields from InSAR data. (a) Ascending and (b) descending LOS ground displacements associated with the $M_w$ 6.3 L'Aquila 2009 event. (c) Ascending and (d) descending LOS ground displacements associated with the $M_w$ 6.5 Norcia 2016 event. (e) Ascending and (f) descending LOS ground displacements associated with the $M_w$ 6.1 Emilia 2012 event.

**Figure S3.** Horizontal and vertical coseismic ground displacements calculated by varying the amplitude of the basal shear tractions (black arrows in Fig. 3) and the along-dip length of the seismogenic fault segment (n. 2 in Fig. 3). Panels (a)–(c) show the effect of the basal shear force, with the length of the seismogenic fault segment maintained at 11.5, 10 and 6 km for the for the L'Aquila 2009, Norcia 2012 and Emilia 2016 earthquakes, respectively. Panels (d) and (e) show the effect of different length of the seismogenic fault segment (n. 2 in Fig. 3), with the amplitude of the shear traction maintained equal to 1.5, 4 and 1.5 MPa for the L'Aquila 2009, Norcia 2016 and Emilia 2012 events, respectively.

**Figure S4.** Plots of the lithostatic vertical stress distribution for the L'Aquila 2009 earthquake case study. (a) Vertical stress distribution without topography. (b) Vertical stress distribution with topography. Negative stresses are compressive. (c) Difference between vertical stress with (panel b) and without (panel a) topography. Negative values indicate stress increase, positive values indicate stress decrease.

**Figure S5.** Plots of the lithostatic horizontal stress distribution for the L'Aquila 2009 earthquake case study. (a) Horizontal stress distribution without topography. (b) Horizontal stress distribution with topography. Negative stresses are compressive. (c) Difference between horizontal stress with (panel b) and without (panel a) topography. Negative values indicate stress increase, and positive values indicate stress decrease.

**Figure S6.** Effect of interseismic basal shear only (i.e. without the contribution of the gravity force) for cross-section 2 of the Nor-cia 2016 earthquake. (a) Modelled differential horizontal stresses. The red lines identify the modelled fault segments. (b) Modelled differential horizontal strains. (c) Modelled differential horizontal displacement pattern and vectors. (d) Comparison between the modelled horizontal velocities (blue curve) and those observed from GPS data (red circles) projected along section 2 assuming a distance from the cross-section of 40 km.

**Figure S7.** Effect of interseismic basal shear only (i.e. without the contribution of the gravity force) for cross-section 3 of the Emilia 2012 earthquake. (a) Modelled differential horizontal stresses. The red line identifies the modelled fault segment. (b) Modelled differential horizontal strains. (c) Modelled differential horizontal displacement pattern and vectors. (d) Comparison between the modelled horizontal velocities (blue curve) and those observed from GPS data (red circles) projected along section 3 assuming a distance from the cross-section of 40 km.

**Data Set S1.** Nodal values of the modelled displacements for the L'Aquila 2009 earthquake.

**Data Set S2.** Nodal values of the modelled strain tensor for the L'Aquila 2009 earthquake.

**Data Set S3.** Nodal values of the modelled stress tensor for the L'Aquila 2009 earthquake.

**Data Set S4.** Nodal values of the modelled displacements for the Norcia 2016 earthquake.

**Data Set S5.** Nodal values of the modelled strain tensor for the Norcia 2016 earthquake.

**Data Set S6.** Nodal values of the modelled stress tensor for the Norcia 2016 earthquake.

**Data Set S7.** Nodal values of the modelled displacements for the Emilia 2012 earthquake.

**Data Set S8.** Nodal values of the modelled strain tensor for the Emilia 2012 earthquake.

**Data Set S9.** Nodal values of the modelled stress tensor for the Emilia 2012 earthquake.

Please note: Oxford University Press is not responsible for the content or functionality of any supporting materials supplied by the authors. Any queries (other than missing material) should be directed to the corresponding author for the paper.